Journal of *Marine Science and Engineering*

MDPI

Article

Modelling, Linearity Analysis and Optimization of an Inductive Angular Displacement Sensor Based on Magnetic Focusing in Ships

Zhipeng Li, Bonan Wang *, Xianbin Wang, Chao Zhang and Xu Meng

School of Traffic and Transportation, Northeast Forestry University, Harbin 150040, China; lizp-nefu@nefu.edu.cn (Z.L.); xbwang10@l63.com (X.W.); 15663712907@163.com (C.Z.); mengxu2016@nefu.edu.cn (X.M.)

* Correspondence: wangbonan126@126.com

Abstract: A sensor for measuring the crankshaft angle of the main engine in ships is designed. Compared with the existing crankshaft angle encoder, this design's advantage is that there is no need to add a gear system at the free end of the crankshaft, reducing machining complexity. The purpose of providing high angle resolution over a wide speed range is achieved. Inductive angular displacement sensors (IADSs) require an eddy current magnetic field as a medium to generate the induced voltage. The induced voltage also requires a complex linearization calculation to obtain a linear relationship between angle and voltage. Therefore, a model of the inductive angular displacement sensor based on magnetic focusing (IADSMF) is proposed. Magnetic focusing is introduced into the IADS to replace the eddy current magnetic field with a focusing magnetic field. The main disadvantage of traditional IADSs, which is that they cannot reduce the eddy current magnetic field, is mitigated. An approximate square−shaped focusing magnetic field (12.4 × 12.4 mm^2) is formed using the magnetic field constraint of the magnetic conductor. When the receiving coil undergoes a position change relative to the square−shaped focusing magnetic field, the voltage generated via the receiving coil is measured using the electromagnetic induction principle to achieve angular displacement measurement. A mathematical model of the IADSMF is derived. Induced voltages at different frequencies and rotational speeds are simulated and analyzed via MATLAB. The results show that frequency is the main factor affecting the induced voltage amplitude. The sensitivity of the IADSMF is 0.2023 mV/°. The resolution and measurement of the IADSMF range from 0.06° and 0–360°. Compared with a conventional planar coil−based IADS, the eddy current loss is reduced from 2.1304 to 0.3625 W. Direct linearization of the angular displacement with the induced voltage is achieved through designing a square−shaped focusing field and receiving coil. After optimizing the sensor structure with the optimization algorithm, the linearity error is 0.6012%. Finally, this sensor provides a theoretical basis and research ideas for IADS development in ships and navigation.

Keywords: crankshaft angle of marine main engines; angular displacement sensor; magnetic focusing; induced voltage analysis; linearity error optimization; eddy current loss

Citation: Li, Z.; Wang, B.; Wang, X.; Zhang, C.; Meng, X. Modelling, Linearity Analysis and Optimization of an Inductive Angular Displacement Sensor Based on Magnetic Focusing in Ships. *J. Mar. Sci. Eng.* **2023**, *11*, 1028. https://doi.org/10.3390/jmse11051028

Academic Editor: Rafael Morales

Received: 25 April 2023
Revised: 8 May 2023
Accepted: 10 May 2023
Published: 11 May 2023

1. Introduction

With the rapid development of sensor technology, angular displacement sensors have become an important research direction. The detection of angular displacement is related to the performance of ship systems and offshore platforms, as expressed in terms of energy consumption, service life and safety [1–4]. The detection of angular displacement plays an important role in modern ships, navigation and ocean transportation [5,6].

Angular displacement measurement is widely used in the shipbuilding industry [7,8] to provide an estimation of the ship test [9], ship turning performance [10], underwater

transmission [11], localization and detection of targets in underwater [12], mooring lines [13] and a berthing assistant system [14].

Currently, most of the propulsion systems used in ships are driven using diesel engines. Most of the diesel engines are manufactured under license from MAN Diesel and Wärtsilä Corporation, which are the world's largest marine diesel engine manufacturers. Crankshaft angle sensor is an important part of the main engine. It provides crankshaft position information to the electronic control unit (ECU) for the purpose of starting the main engine and controlling the injection timing, injection volume, injection pressure and opening and closing of the exhaust valve.

The gear at the free end of the main engine of the ship has hundreds of teeth, and the crankshaft angle encoder is above the gear [15]. The encoder gives a rectangular voltage signal due to the change in gear air gap. This tool records the number of high and low electrical levels, and the final measurement of the angular position is achieved. The system has several disadvantages: (1) the crankshaft has to be machined with teeth; and (2) if a higher resolution is needed, the gear should be reprocessed.

Angle, torque and power are important control parameters in ship propulsion systems. They determine whether the ship can operate normally, as well as its fuel consumption and safety. It is necessary to measure and monitor these factors. The torque can be calculated using the torsion angle on the rotating shaft, and the power is calculated using the torque through the formula [16,17]. Thus, the premise of monitoring them is to measure the angle.

The common ways to measure the torque on the main engine are as follows.

(1) Torque is measured through measuring the surface deformation of the rotating shaft during engine operation. The use of strain gauges as sensors is one of the most common [15]. Four half-bridge strain gauges are affixed directly to the rotating shaft. The measurement principle for torque is based on the relationship between shear stress and normal stress for pure torsion. The torque is then calculated using Equation (1):

$$M = \frac{\varepsilon}{\pi \cdot G r^3}, \tag{1}$$

where M—torque, ε—strain, G—shear modulus and r—shaft radius.

(2) This method is based on an optical sensor and, through two teeth fixed on the shaft, the distance is "1" teethed rings, achieving torque measurement. This measurement method requires only one optical sensor [18]. The relationship between teethed rings is proportional to the torsion angle of the shaft. When no torque is applied to the shaft, the torsion angle $\varphi = 0$. At this time, the pulse period T_1 and T_2 of the two tooth rings corresponding to the optical sensor are equal. When there is a torque applied to the shaft, $\varphi \neq 0$ and $T_1 \neq T_2$. The torque is then calculated using Equation (2):

$$M = \frac{k_T \cdot (T_1 - T_2)}{n}, \tag{2}$$

where k_T—coefficient depends on construction of shaft and teethed wheels, n—revolution and T_1, T_2—time of pulses received from optical sensor.

There are several disadvantages of using this method (1): the measurement method of strain gauge is contact measurement, and contact friction due to long-term use will cause the measurement results to deteriorate; (2): a geared system is required, and the number of teeth of the gearing after processing is fixed. Thus, machining becomes more difficult as the resolution of the measurement angle increases.

Therefore, this paper proposes an inductive angular displacement sensor based on magnetic focusing (IADSMF) to replace the crankshaft angle encoder. The aim of this study is to provide high angular resolution over a wide speed range without using machining tooth rings. Furthermore, through adding an IADSMF to the other end of the shaft, the torsion angle φ and torque of the shaft system can be measured [17]. Not only

does the sensor have the function of measuring angles, but it can also be extended to measure torque. [15] mentioned that the cost of measuring shaft torque is five times higher than measuring angular displacement in a ship's main engine system. As a result, versatility is addressed while measurement costs are reduced.

1.1. Related Work

1.1.1. Angular Displacement Sensor

According to how angular displacement measurement is implemented, angular displacement sensors can be divided into contact and non−contact sensors. Traditional contact sensors are mainly potentiometric and resistance strain sensors [19–21]. The main disadvantages are contact friction, large differences in measurement results due to the attachment process, limited resolution, and strain gauge creep after long-term use. These problems can lead to increased wear, affecting measurement accuracy and service life.

Non−contact sensors mainly include optical sensors, capacitive sensors [22,23], magneto−resistive sensors [24–26] and inductive sensors [27,28]. Optical sensors are categorized as photoelectric encoders [29–31] or grating sensors [32-34]. Their advantages are high measurement resolution and accuracy. Their disadvantages [35] are structural complexity and expense. They also have special requirements in specific environments. Their disadvantages limit their application in measurement. Capacitive sensors [22] have the advantages of high sensitivity, such as a simple structure and small non−linear error, but the disadvantages are evident. For example, capacitive sensors are prone to parasitic capacitance, leading to low measurement accuracy and poor load capacity that is susceptible to external interference, affecting sensor stability. Magneto−resistive sensors [24,25] are sensitive to changes in orientation over an angular measurement range of 0–180°. Their measurement results are more accurate than those of potentiometric sensors, and they are widely used in automotive pedal detection. However, the anisotropy of their magneto−resistive shapes can cause harmonic distortion, which affects measurement.

An inductive angular displacement sensor (IADS) is an electromagnetic sensor [27,36–38] that typically uses a printed circuit board (PCB) to support a stator and rotor made from a metal sheet. The stator contains an excitation coil and m receiving coils. The physical space angle difference of each receiving coil is 1/m of the angle corresponding to a measurement period, where the m value is generally 3. The excitation coil generates a magnetic field, and rotation of the rotor causes electromagnetic induction between the rotor and receiving coil. The change in position causes the receiving coil to produce an induced voltage. The magnitude of the induced voltage depends on the rotor position, allowing measurement of the angular displacement. An IADS has the following advantages; (1) it has a simple structure and no friction loss, no parasitic capacitance, a moderate price, and no special requirements for operating environments; (2) the sensor is composed of PCBs and metal sheets without additional materials; (3) the measuring range of angular displacement can reach 360°, which is larger than that of a magneto−resistive sensor.

Table 1 shows the advantages and disadvantages of non−contact angular displacement sensors. In summary, the IADS is an ideal sensor for engineering applications. IADS is especially suitable for the harsh environment of navigation ships, which are characterized by high temperatures, humid air, poor ventilation and high salinity gas erosion.

Table 1. Advantages and disadvantages of non−contact angular displacement sensors.

	Optical	**Magneto−resistive**	**Capacitive**	**Inductive**
Measurement range	0–360°	0–180°	0–360°	0–360°
Output is linear or not	No	No	Yes	Yes
Measurement resolution	0.35°	0.08°	0.1°	0.15°
Manufacturing difficulty	Harder	Moderate	Moderate	Simple
External environmental impact	Large	Small	Moderate	Small

1.1.2. Magnetic Focusing and Application

Magnetic focusing in magnetism is the spiral line motion of charged particles in a magnetic field. It is implemented when a charged particle beam enters uniform magnetic field B with an initial velocity v. Moreover, the angle between v and B is small, with $v_{//} = v\cos\theta \approx v$, $v_{\perp} = v\sin\theta \approx v\theta$. Thus, each particle has a spiral motion. Since the $v_{//}$ of each particle is almost the same, the pitch is approximately equal. Therefore, particle beams converge at the same point after completing the spiral motion.

With the development of technology, material processing techniques using focus−adjustable laser beams and electron beams as high−energy density heat sources emerged in the field of magnetics. Among them, high−energy electron beam processing technology has the advantages of a vacuum environment and high energy utilization rate, and was applied to metal additive manufacturing technology [39]. In recent years, the use of the above−mentioned particle beam motion drove technological developments in the microscopic field, such as the processing of microscopic materials [40,41]. Moreover, the technology's application for electron microscopes and scanning electron microscopes are growing [42,43].

Magnetic focusing is generally achieved using the magnetic field excited in a current-carrying solenoid. In most practical applications, the non−uniform magnetic field excited via the coil is commonly used to achieve magnetic focusing. Magnetic focusing has long been used in physics and medicine. For example, Siegbahn et al. [44] studied the focusing of two−dimensional electrons in an inhomogeneous magnetic field. Walton et al. [45] used a uniform magnetic field with a straight−line boundary for high−order focusing, enabling a mass spectrograph to better separate and detect charged ions. Damadian et al. [46] visualized tumours in living animals through field-focusing nuclear magnetic resonance (FONAR). In recent years, magnetic focusing was widely used in transcranial magnetic stimulation [47] (TMS), magnetic resonance imaging [48], magnetic drug targeting [49–51] (MDT), underground pipeline localization [52], metal soldering [53], metal surface detection [54] and quantum science [55].

Traditionally, the TMS magnetic focusing process used a figure−eight coil [56], double−butterfly coil [57] or other structures [58]. Following years of development, TMS can now be used to activate neurons [59], thus playing a vital role in the treatment of neurological disorders and rehabilitation. Philip et al. [60] reported on the use of TMS to stimulate tissues, such as the amygdala, deep in the brain. This study involved the treatment of advanced brain stimulation. TMS based on magnetic focusing has even made positive contributions in stuttering improvement [61] and detoxification [62]. The localization and image acquisition of cerebral haemorrhages in patients was achieved via portable magnetic resonance imaging [48]. While simplifying the detection process, TMS reduces the potential risk of patients exposed to a high−intensity magnetic field environment. MDT [50] is a process that uses the magnetic force of an external focusing magnetic field to remotely deliver a drug containing magnetic particles to a lesion site. Non−invasive or minimally invasive drug therapy was achieved through MDT, avoiding the potential risks associated with surgery.

Using the magnetic focusing method (MFM) [63], a relatively high magnetic field can be formed in a tiny area on an outer metal surface using the needle tip of a magnetic conductor (MC). When the MC scans a metal surface with defects, the stable magnetic field is disturbed and changed. The induced signal in the outer coil of the MC is made to change, and metal surface defect detection is realized. The MFM, thus, became a mainstream non-destructive testing method. Chen et al. [55] simplified quantum processing devices using ultra−high enhanced field–matter interaction generated via magnetic focusing. This study promoted the application of magnetic focusing in integrated quantum information processing and high−sensitivity quantum sensing.

In summary, magnetic focusing is widely used in medicine, equipment testing, materials science and quantum science. To the best of our knowledge, it is less commonly used in measurement applications, especially in angular displacement sensors with ships.

1.2. Contribution

The main contributions of this paper are as follows.

(1) An IADS based on the MFM is proposed. A breakthrough in the measurement method of the IADS is realized. Compared with the existing crankshaft angle sensors in the ship, the angle resolution is improved. The angular resolution is improved from the existing 0.35 or 0.5 degrees to 0.06 degrees when the speed is 100 r/min.

(2) A mathematical model of the proposed sensor is derived, and the accuracy and feasibility of the sensor are verified theoretically via simulations.

(3) Direct linearization of the induced voltage and angular displacement is realized using this sensor. Compared with the traditional IADS case, there is no need for linearization design and calculation. The corresponding linearization error is only 0.6239%.

(4) The sensor has a lower eddy current loss than the traditional IADS. The eddy current loss is reduced from 2.103 W to 0.3625 W.

2. Methods and Models

2.1. Excitation Methods and Sensor Modelling

The common excitation methods for magnetic focusing and IADS are shown in Table 2. As shown in Table 2, most of the traditional focusing methods are two−dimensional planes or combinations of coil arrays. They only complete the coil to focus the magnetic field at a point below it, achieving an increase in the magnetic field at only one point. The magnetic field and its magnetic flux leakage in a certain area of the plane is ignored. Based on this defect and combined with the excitation method of IADS, this paper proposed the combination of Archimedes coil, hollow−core MC and solid−core MC. Due to the emergence of hollow− and solid−core MC, the focusing effect was increased and the surrounding magnetic flux leakage was reduced. Focusing was achieved in a certain area below the MC. The magnetic flux leakage outside the area was reduced to a negligible level, and this method was used to meet the measurement requirements of IADSMF.

Table 2. Magnetic focusing and IADS excitation method.

	Magnetic Focusing	IADS	IADSMF
Excitation method	Figure−eight coil [56]	Circular coil [27, 64]	Archimedes coil, hollow−core MC and solid−core MC
	Double−butterfly coil [57]	Semicircular arc coil [65]	
	Hemispherical solenoid array [66]	Four square Archimedes coils [67]	
	C−type core coil [68]	Planar spiral coil [69]	
	Coil arrays in hemispherical, plane and torus shapes [70]	-	
	Biconical stimulation coil system [71]	-	

The sensor was modeled using the modelling function that came with COMSOL software. The sensor model is shown in Figure 1. The modelling parameters are shown in Table 3. The sensor stator was composed of two Archimedes coils, a solid−core MC and two hollow−core MCs. The Archimedes coil was arranged on the PCB. Two PCBs arranged with Archimedes coils were taped to each end of a solid−core MC (see Figure 1 for a schematic of the sensor structure). The Archimedes coil was used as an excitation source for generating a magnetic field. The functions of the solid−core MC were to conduct magnetism and constrain the Archimedes coil. The PCB with Archimedes coil was adhered to solid−core MC surface to prevent detachment. Constraining the magnetic field and reducing magnetic flux leakage were the roles of the hollow−core MC as a magnetic conduction device and shielding layer. The cross−section of the hollow−core MC was square−shaped; thus, the Archimedes coil on the inner wall was located 1 mm below the bottom, generating a square−shaped magnetic field (12.4 × 12.4 mm^2).

A flexible printed circuit (FPC) had characteristics of arbitrary bending, and FPC technology was used to manufacture the receiving coil. An FPC was wound on the surface

of the shaft to realize the requirement of the receiving coil being wound around the shaft. Through wrapping the FPC around the shaft, the need for the rotor to wrap around the shaft circumference was satisfied. The receiving coil in the FPC was square−shaped, and the position of one coil between two adjacent receiving coils was empty. The size of the receiving coil was the same as that of the square−shaped magnetic field. The rotor consists of 12 receiving coils with a difference of 15° between adjacent receiving coils. These dimensions represented the overall structural design of the sensor detailed in this subsection. Through focusing the magnetic field, the direct linearization of the induced voltage and angular displacement and sensor loss reduction can be realized via this design.

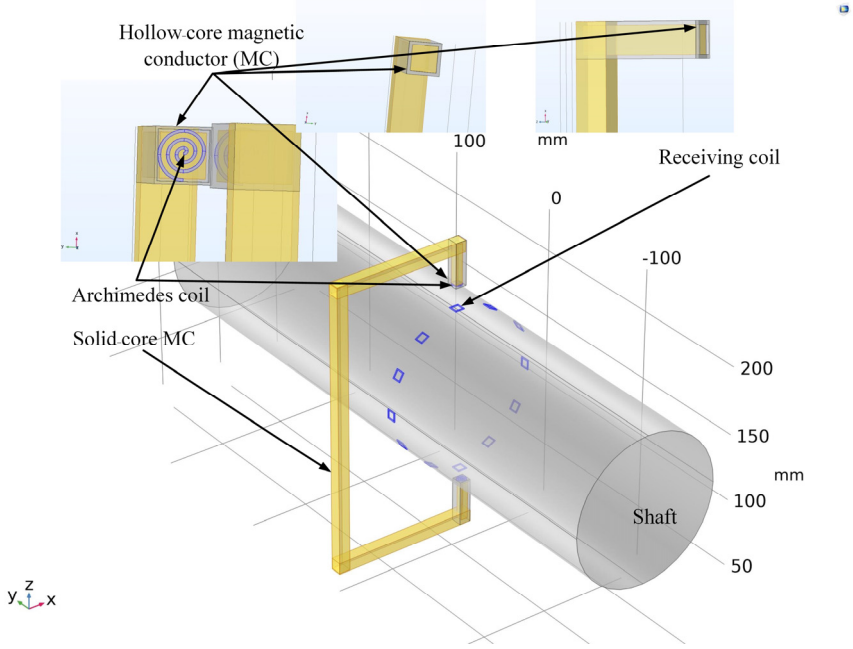

Figure 1. Sensor structure diagram.

Table 3. The modelling parameters.

Parameter Name	Value (mm)	Material
Radial side length of solid−core MC	8	Iron
Radial thickness of hollow−core MC	1	Iron
Maximum radius of Archimedes coil	4	Copper
Receiving coil side length	12.4	Copper
Radius of rotating shaft	47.4	Iron

2.2. Receiving Coil Structure Arrangement

The planar structure of the FPC receiving coils was designed as shown in Figure 2a. The FPC had 4 layers. Odd receiving coils were arranged in the first layer, and even receiving coils were arranged in the second layer (Figure 2b). Wires connected to odd coils were arranged in the third layer, and wires connected to even coils were arranged in the fourth layer.

The induced currents in odd coils, such as receiving coils 1 and 3, moved in the same direction, while the induced currents in even coils, such as receiving coils 2 and 4, also moved in the same direction. The induced current directions of the odd and even receiving coils were opposite. The odd coil and even coils were connected to form a complete set of receiving coils. Black circles indicate the position of the over-holes between the different layers (Figure 2a). Every over−hole position had a small offset from the receiving coil of this layer, which ensured that the two sides of the same receiving coil did not overlap.

The red arrow represents the current direction. The blue line represents the winding method of the odd receiving coils. The green line represents the winding method of the even receiving coils. The red line represents the winding method of connecting the receiving coil wires (Figure 2b). In Figure 2b, the small offset of the over-hole is enlarged for clarity.

The spatial arrangement was such that the center points of all receiving coils were located on the same axis (*X*−axis), allowing the receiving coils on the shaft surface to be arranged stably for one week. We noted that to show the staggered relationship between the receiving coil and the wire, the center point of the receiving coil (shown in Figure 2a) was not on the same axis (*X*−axis). However, the center points of the actual FPC receiving coils were on the same axis.

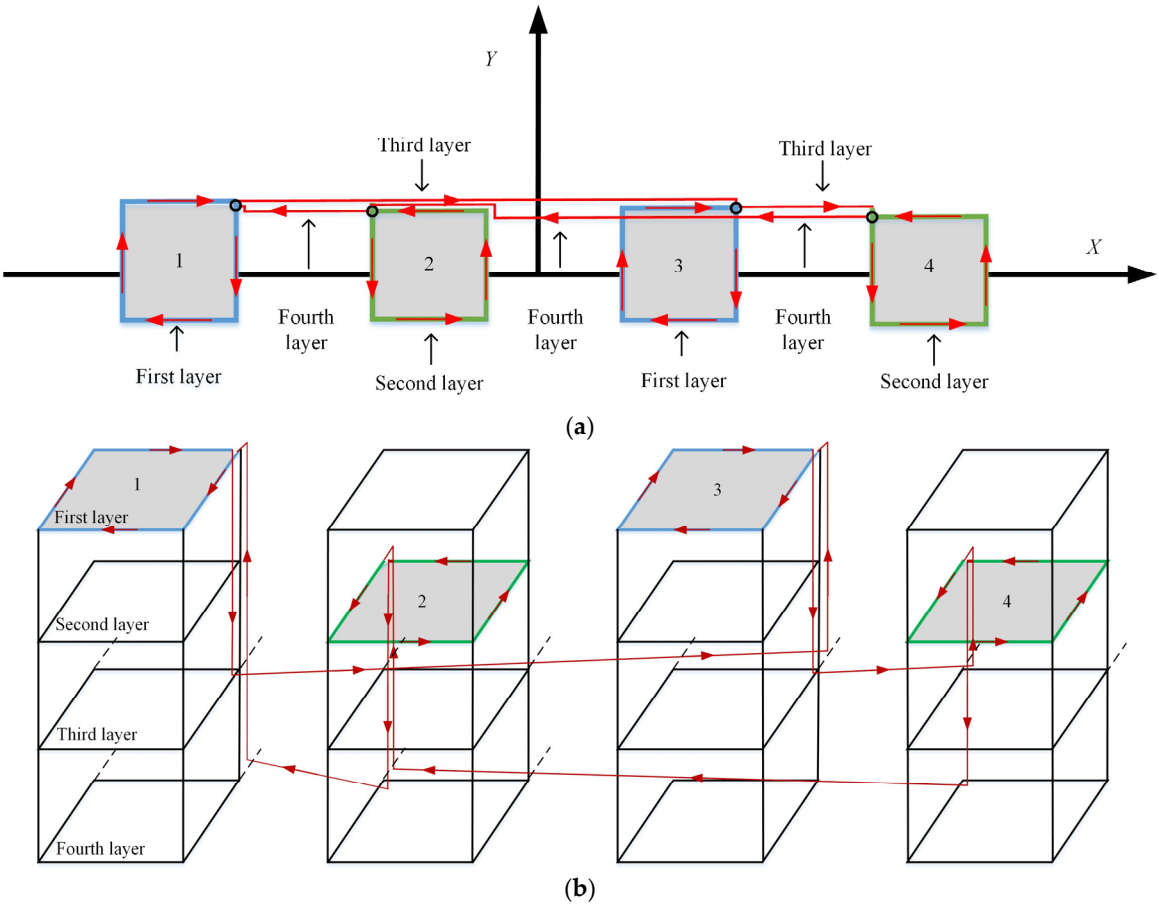

Figure 2. FPC receiving coil plane connection diagram: (**a**) two-dimensional diagram; (**b**) three-dimensional diagram.

2.3. Measurement Principle and Mathematical Modelling

2.3.1. Measurement Principle of Angular Displacement

According to the principle of electromagnetic induction, the induced voltage u [72] can be expressed as in (3):

$$u = -N\frac{d\psi}{dt} = -N\frac{d}{dt}\boldsymbol{B}_z \cdot S\,, \tag{3}$$

where ψ and N represent the magnetic flux and the turn number, respectively; $\boldsymbol{B}_z$ is the magnetic flux density in the *Z*−axis direction; and S is the receiving coil area.

A stable focusing magnetic field (square) was formed using the MFM, and the receiving coil shape was the same as it (Figure 3). When the focusing magnetic field did not

coincide with the receiving coil (position 1), there was no magnetic field in the area enclosed using the receiving coil; thus, the magnetic flux was zero. When the shaft rotated, the area where the receiving coil coincided with the focusing magnetic field increased, and the magnetic flux began to increase (the receiving coil was between positions 1 and 2). When the focusing magnetic field reached position 2, the receiving coil completely coincided with the focusing magnetic field, and the negative magnetic flux was maximum. The receiving coil continued to move. When the focusing magnetic field was between positions 2 and 3, the overlap area between the receiving coil and the focusing magnetic field decreased. When the focusing magnetic field reached position 3, the magnetic flux was 0. When the focusing magnetic field reached between 3 and 4, the positive magnetic flux began to increase. When the focusing magnetic field reached position 4, the receiving coil coincided completely with the focusing magnetic field for the second time, and the positive magnetic was maximum (the magnetic flux at position 2 was opposite to that at position 4, which was achieved through winding the receiving coil, as shown in Figure 2). When the focusing magnetic field was located between positions 4 and 5, the overlap area between the receiving coil and the focusing magnetic field decreased, and the forward magnetic flux decreased. When the focusing magnetic field reached position 5, the receiving coil did not coincide with the focusing magnetic field, and the magnetic flux was 0.

The process of measuring angular displacement was the process of changing receiving coils on the rotor with respect to the Archimedes coil via a corresponding angle. The rotor rotated one measurement period (60°), and the corresponding change in the magnetic flux of receiving coils for a period was $0 \to -\psi \to 0 \to \psi \to 0$. According to the principle of electromagnetic induction, the receiving coil generated the induced voltage for one cycle as follows: $0 \to u \to 0 \to -u \to 0$. The relationship between the induced voltage of the receiving coils and the shaft angular displacement was approximately a sine wave (Figure 3).

A linear relationship between the induced voltage and angular displacement was induced using the FPC receiving coils, enabling the measurement of angular displacement (Figure 3). The difficulty of sensor design and linearization calculation was reduced through the linear relationship between angular displacement and induced voltage. The sensor had the advantages of being easy to calibrate, avoiding non−linear compensation and being easy to analyze.

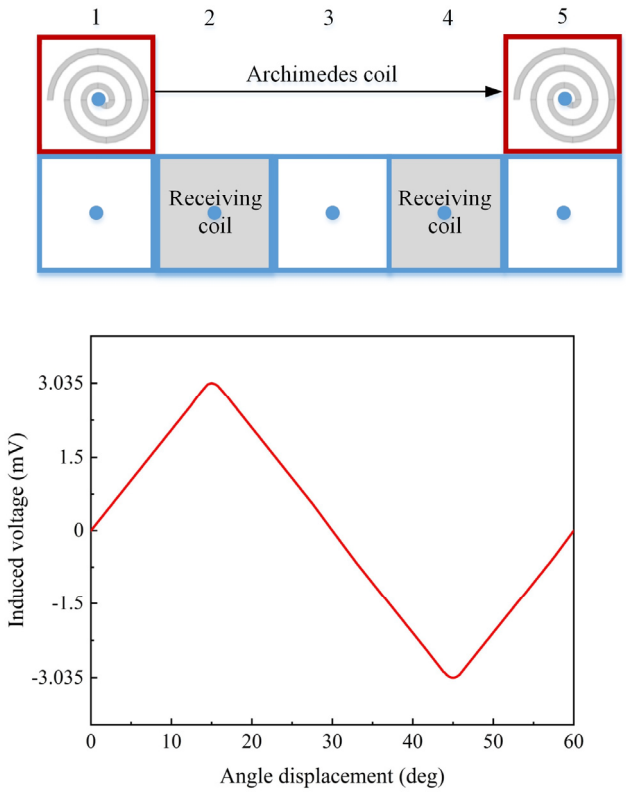

Figure 3. Induced voltage of receiving coils over one cycle.

For the induced voltage analysis, mathematical modelling of $\boldsymbol{B}_z$ and S was performed first, and the simulation analysis was carried out.

2.3.2. Archimedes Coil Magnetic Field Model

The Archimedes coil polar coordinate [73,74] is shown in Equation (4):

$$R = a + b\theta\,, \tag{4}$$

where a is the initial radius, b is the coil pitch and θ is the rotation angle. Equation (4) is expanded into parametric Equation (5) (Figure 4a):

$$\begin{aligned} x &= R \cdot \cos\theta \\ y &= R \cdot \sin\theta \end{aligned}\,. \tag{5}$$

The polar coordinate equation is then transformed into the parameter equation in the Cartesian coordinate system. Equation (5) can be described via (6):

$$\begin{aligned} x &= (a + b\theta) \cdot \cos\theta \\ y &= (a + b\theta) \cdot \sin\theta \end{aligned}\,. \tag{6}$$

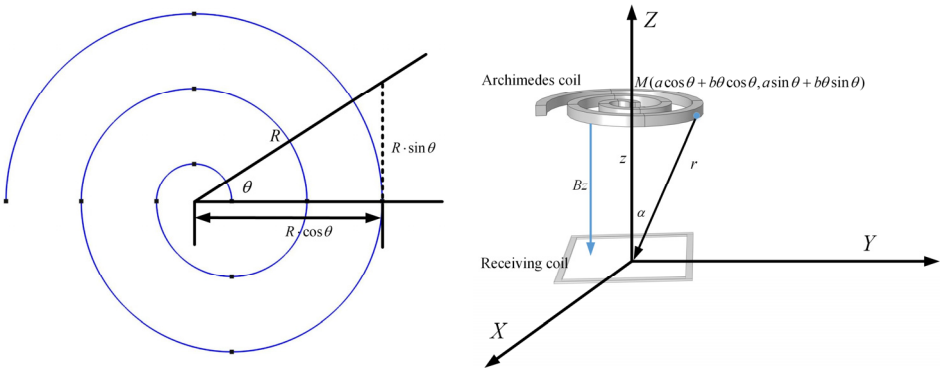

(**a**) (**b**)

Figure 4. Related schematic diagram of Archimedes coil: (**a**) parameter equation diagram; (**b**) generated magnetic field diagram.

The lower magnetic flux leakage was neglected in the theoretical derivation of this paper to reduce the difficulty with theoretical derivation. According to Biot–Savart's law [75], the Archimedes coil with the MC in the Z magnetic flux density generated in the direction was $\boldsymbol{B}_z$ (Figure 4b). $\boldsymbol{B}_z$ can be obtained as follows (7):

$$\begin{aligned} \boldsymbol{B}_z &= \oint_{l_0} d\boldsymbol{B} \cdot \cos\alpha = \int \boldsymbol{B} \cdot \cos\alpha dl_0 = \int \frac{\mu_0 u_r}{4\pi r^2} \cdot \frac{u_1 \cdot \sin(2\pi f_1 t)}{R_1} dl_0 \\ &= \frac{\mu_0 u_r I_1 \cdot \sin(2\pi f_1 t)}{4\pi} \cdot \int_0^{k\cdot 2\pi} \frac{a + b\theta}{(a^2 + b^2\theta^2 + 2ab\theta + z^2)^{3/2}} d\theta \end{aligned}, \quad (7)$$

where l_0 and α represent the circumference of the Archimedes coil and the angle between $\boldsymbol{B}$ and the Z−axis, respectively; u_0 and u_r represent the permeability of vacuum and the MC relative permeability, respectively,; r is the distance from point M on the Archimedes coil to the center of the receiving coil; k and u_1 represent the number of coil loops and the excitation voltage, respectively; R_1 and I_1 represent the Archimedes coil resistance and the excitation current with frequency f_1, respectively; and z is the vertical distance from the Archimedes coil to the receiving plane.

To reduce the difficulty of deriving the equations, the values of $\boldsymbol{B}_z$ at the center point and in the region of the receiving coil are considered to be the same.

2.3.3. Receiving Coil Area Change Model

The three−dimensional space rotation of the Archimedes coil and the receiving coil was simplified into a two−dimensional−plane relative motion (Figure 5). The mathematical model of receiving coil area change was implemented, and the curvature of the receiving coil was neglected both here and subsequently in this study. Here, only the trend of the magnetic flux change from zero to the maximum value is shown, and the trend of the other phases was the same but in different directions.

The red−bordered square shape represents the focusing magnetic field generated using the Archimedes coil (side length is l) in Figure 5. The grey square−shaped coil is the receiving coil with side l. The white square−shaped coil is vacant. The absolute value of x represents the distance between the Archimedes coil and the Y−axis. The length of the Archimedes coil coinciding with the receiving coil is equal to $l - |x|$. The overlap area of the Archimedes coil and the receiving coil can be expressed as $S(x) = l \cdot (l - |x|)$, $x \in (-l, +l)$.

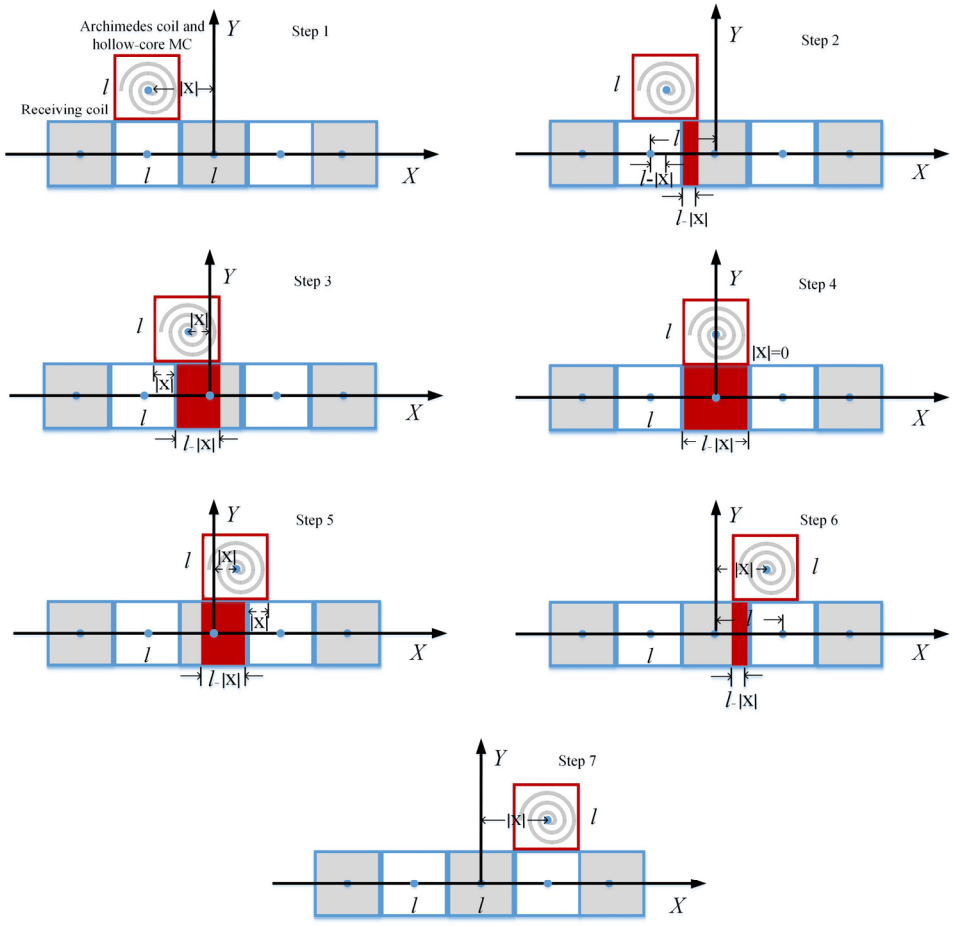

Figure 5. Relative motion diagram of coils.

The Fourier expansion of $S(x)$ [76,77] and $S(x)$ is an even function. $S(x)$ can be described via (8)–(10):

$$S(x) = \frac{a_0}{2} + \sum_{n=1}^{\infty}\left(a_n \cos\frac{n\pi x}{l}\right), \tag{8}$$

$$a_0 = \frac{2}{l}\int_0^l l\cdot(l-x)dx = \frac{l\cdot x(2l-x)}{l}\Big|_0^l = l^2, \tag{9}$$

$$\begin{aligned} a_n &= \frac{2}{l}\int_0^l l\cdot(l-x)\cdot\cos\frac{n\pi x}{l}dx = \frac{2l\cdot(l-x)}{n\pi}\sin\frac{n\pi x}{l} - \frac{2l^2}{n^2\pi^2}\cos\frac{n\pi x}{l}\Big|_0^l, \\ &= -\frac{2l^2}{n^2\pi^2}(\cos n\pi - 1) = \frac{2l^2}{n^2\pi^2}(1-\cos n\pi) = \frac{4l^2}{n^2\pi^2}\cdot(\sin\frac{n\pi}{2})^2 \end{aligned} \tag{10}$$

where the fundamental wave period is $l = \frac{2\pi R_a}{N_1}$.

The angular displacement y can be obtained via (11):

$$y = vt = \omega R_a t = \frac{2\pi n_a R_a t}{60}, \tag{11}$$

where v and ω represent the linear velocity of the receiving coil and the angular velocity of the receiving coil, respectively; R_a and n_a represent the radius of the shaft and the rotational speed of the receiving coil, respectively; and N_1 is twice the number of receiving coils.

$$S(x) = \frac{a_0}{2} + \sum_{n=1}^{\infty}\left(a_n \cos\frac{n\pi x}{l}\right) = \frac{l^2}{2} + \sum_{n=1}^{\infty}\frac{4l^2}{n^2\pi^2}\cdot\left(\sin\frac{n\pi}{2}\right)^2 \cdot \cos\frac{nN_1\pi n_a t}{60}, \tag{12}$$

where n is the number of Fourier expansion terms.

2.3.4. Receiving Coil Induced Voltage Model

The induced voltage model was derived in this subsubsection. To avoid confusion, the excitation voltage generated using the Archimedes coil is set to u_1, and the induced voltage of the receiving coil is set to u_2. According to Lenz's law [72], u_2 can be obtained via (13):

$$u_2 = -n_2\frac{d\psi}{dt} = -n_2\frac{d}{dt}\boldsymbol{B}_z \cdot S. \tag{13}$$

The frequency−independent terms are set as coefficients (K_1, K_2 and K_3) in the expression to highlight the relationship between frequency and induced voltage in the equation. K_1, K_2 and K_3 can be obtained via (14), (15) and (16):

$$K_1 = \frac{\boldsymbol{B}_z}{\sin(2\pi f_1 t)} = \frac{\mu_0\mu_r I_1}{4\pi}\cdot\int_0^{k\cdot 2\pi}\frac{a+b\theta}{(a^2+b^2\theta^2+2ab\theta+z^2)^{3/2}}d\theta, \tag{14}$$

$$K_2 = \frac{a_0}{2} = \frac{l^2}{2}, \tag{15}$$

$$K_3 = a_n = \frac{4l^2}{n^2\pi^2}\cdot\left(\sin\frac{n\pi}{2}\right)^2. \tag{16}$$

Here, u_2 is split into three expressions for the excitation frequency f_1, and u_2 is shown in (17). Thus, u_{21}, u_{22} and u_{23} can be obtained via (18), (19) and (20):

$$u_2 = u_{21} + u_{22} + u_{23}, \tag{17}$$

$$u_{21} = -n_2 K_1 K_2 \cdot \cos(2\pi f_1 t)\cdot 2\pi f_1, \tag{18}$$

$$u_{22} = -n_2\sum_{n=1}^{\infty}K_1 K_3 \cdot \cos\frac{nN_1\pi n_a t}{60}\cdot\cos(2\pi f_1 t)\cdot 2\pi f_1, \tag{19}$$

$$u_{23} = -n_2\sum_{n=1}^{\infty}K_1 K_3 \cdot \sin(2\pi f_1 t)\cdot\left(-\frac{nN_1\pi n_a}{60}\cdot\sin\frac{nN_1\pi n_a t}{60}\right). \tag{20}$$

The final expression for u_2 can be described via (21):

$$\begin{aligned} u_2 &= -n_2K_1K_2\cdot\cos(2\pi f_1t)\cdot 2\pi f_1 - n_2\sum_{n=1}^{\infty}K_1K_3\cdot\cos\frac{nN_1\pi n_a t}{60}\cdot\cos(2\pi f_1t)\cdot 2\pi f_1 - n_2\sum_{n=1}^{\infty}K_1K_3\cdot\sin(2\pi f_1t)\cdot\left(-\frac{nN_1\pi n_a}{60}\cdot\sin\frac{nN_1\pi n_a t}{60}\right) \\ &= -n_2\left[K_1K_2\cdot 2\pi f_1 + \sum_{n=1}^{\infty}K_1K_3\cdot\cos\frac{nN_1\pi n_a t}{60}\cdot(2\pi f_1t - \frac{nN_1\pi n_a}{60})\right]\cdot\cos(2\pi f_1t) - n_2\sum_{n=1}^{\infty}K_1K_3\cdot\frac{nN_1\pi n_a}{60}\cdot\cos(2\pi f_1 + \frac{nN_1\pi n_a}{60})t \end{aligned} \quad (21)$$

For a concise and clear representation of the effect of excitation frequency and rotational speed on the induced voltage, the initial Equation (3) for the induced voltage is expressed in (24), where the excitation current $i(t)$ is described via (22):

$$i(t) = I\cdot\sin(\omega t)\,. \quad (22)$$

The magnetic flux of the receiving coil can be obtained as follows (23):

$$\psi = k_4 y\sin(\omega t), \quad (23)$$

where k_4 is the proportionality factor and y is the angular displacement.

Equations (22) and (23) are substituted into Equation (3) to obtain (24):

$$\begin{aligned} u &= -N\frac{d\psi}{dt} = -N\frac{d\left[k_4 y\sin(\omega t)\right]}{dt} = -Nk_4\frac{dy}{dt}\cdot\sin(\omega t) - Nk_4 y\omega\cdot\cos(\omega t) \\ &= -Nk_4 v\cdot\sin(\omega t) - Nk_4 y\omega\cdot\cos(\omega t) = -Nk_4\sqrt{v^2 + (y\cdot 2\pi f_1)^2}\cdot\sin(2\pi f_1 t + \varphi) \end{aligned}\,. \quad (24)$$

At f_1 = 10 kHz, the linear velocities of 5.6 m/s and 5.6 × 10^{-3} m/s, corresponding to 1000 r/min and 1 r/min, respectively, are substituted into Equation (24), and the ratio is then calculated. The induced voltage amplitude is increased by a factor of merely 1.000023 when the rotational speed is increased from 1 r/min to 1000 r/min. Therefore, when the rotational speed change value is less than 1000 r/min, the induced voltage change is very small and can be directly ignored. From Equation (24), it can be seen that the magnitude of the excitation frequency is the main factor affecting the induced voltage amplitude when the excitation frequency is in the kHz range. Only when the rotational speed increases to 10^4 r/min does the rotational speed affect the induced voltage amplitude, with the amplitude increasing by a factor of 1.002; however, the impact is still small.

3. Results

3.1. Verification and Analysis of the Focusing Magnetic Field

COMSOL software is used to simulate the Archimedes coils with and without an MC. The two sets of Archimedes coils are separately fed with an excitation voltage of 10 mV to verify whether the above non−MC and MC setups can generate a square−shaped focusing magnetic field. This set−up provides a basis for the next step to measure the dynamic induced voltage. A circular magnetic field with a diameter of 20 mm is formed in the *X*-*Y* plane at a distance of 1 mm below it (Figure 6). The magnetic field is in a divergent state without the MC. The ratio of the magnetic flux density of the red circular magnetic field to that of the surrounding blue area is 4.61. This ratio is defined as the magnetic field focusing intensity λ. In engineering, if the value of the same parameter differs by more than one order of magnitude, the lower value can be ignored. The λ_1 value formed without an MC is only 4.61, which cannot meet the measurement requirement of ignoring the surrounding magnetic flux leakage (Figure 6 and Table 4).

The magnetic field is approximately square−shaped (12.4 × 12.4 mm^2), reducing the area by 160.24 mm^2 (Figure 7 and Table 4). The λ_2 value formed by the MC is 11.48, which is greater than an order of magnitude; thus, the magnetic field in the blue region can be ignored (Figure 7).

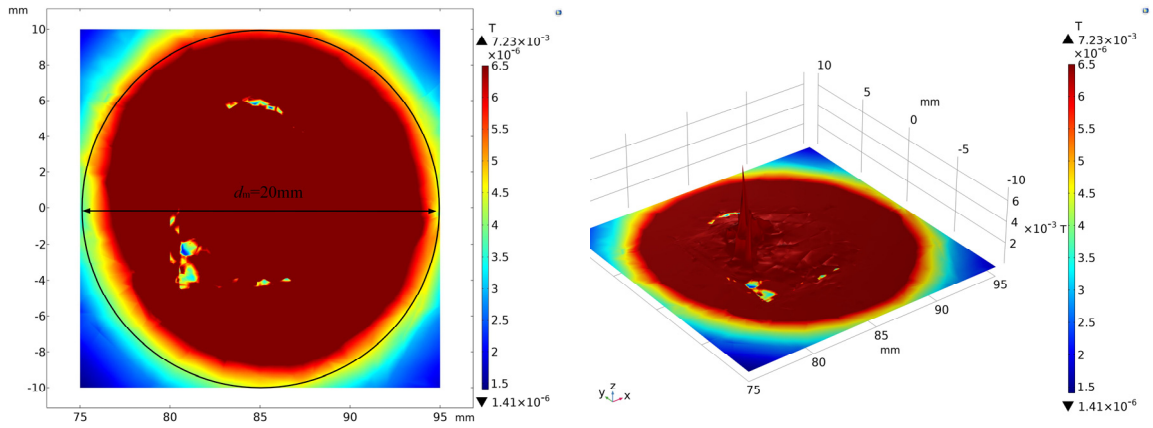

(**a**) (**b**)

Figure 6. Magnetic field 1 mm the Archimedes coil without an MC: (**a**) two−dimensional diagram; (**b**) three−dimensional contour diagram.

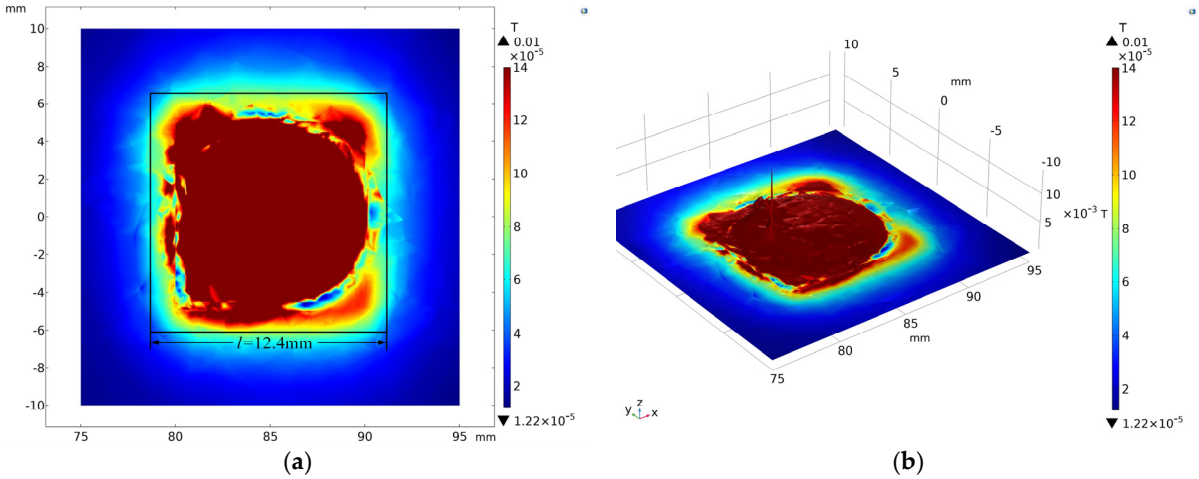

(**a**) (**b**)

Figure 7. Magnetic field 1 mm below Archimedes coil with an MC: (**a**) two−dimensional diagram; (**b**) three−dimensional contour diagram.

Table 4. Parameters obtained via two simulations.

Parameter Name	Magnetic Field without MC	Magnetic Field with MC
Magnetic field diameter, d_m (mm); Magnetic field side length, l (mm)	20	12.4
Magnetic field area, $S_m = \pi(d_m/2)^2$; $S_m = l^2$ (mm²)	314	153.76
Maximum magnetic flux density, $\boldsymbol{B}_{max}$ (T)	7.23×10^{-3}	1×10^{-2}
Focusing magnetic flux density $\boldsymbol{B}_F$ (T)	6.5×10^{-6}	1.4×10^{-4}
Flux leakage, $\boldsymbol{B}_L$ (T)	1.41×10^{-6}	1.22×10^{-5}
Magnetic field focusing intensity, $\lambda = \boldsymbol{B}_F/\boldsymbol{B}_L$	4.61	11.48

We note that the Archimedes coil without an MC is 1 mm above the rotation axis of the ferromagnetic material. Therefore, it can be assumed that the Archimedes coil has an MC, but its relative permeability is not as large. For this reason, the maximum magnetic flux density differs by only one order of magnitude, as shown in Figures 6 and 7. As shown in Figures 6 and 7, only the magnetic field value of the left minimal region is relatively large (1×10^{-2} T), while the other areas have essentially the same value and can be approximately considered to correspond to a uniform magnetic field.

The previous study was focused on a minuscule area, i.e., a point [63]. At this point, there was very little magnetic field that could be emitted independently. Therefore, the relative permeability u_r was changed from 300 to 60,000, and the increase in multiple K after magnetic focusing was not large, being only 1.08 times. Compared with the minuscule area of the previous study, the magnetic focusing area of this paper is large (12.4 × 12.4 mm^2). The original divergent magnetic field in this region is focused; thus, K corresponding to $\boldsymbol{B}_{max}$ and $\boldsymbol{B}_F$ is larger than the multiples of the previous study. However, the increasing trend of K is the same as the previous trend. The corresponding K increases by a factor of 1.38 at the position of $\boldsymbol{B}_{max}$ in this region and by a factor of 21.54 over the entire focusing magnetic field region.

Here, the increased K value is not equal to the relative permeability u_r of the MC for the following reasons: (1) the hollow−core MC can only constrain the magnetic field and cannot completely concentrate all the magnetic flux leakage in the square−shaped area; (2) the lower Archimedes coil is a rotating shaft, which is equivalent to having an MC with a small relative permeability. Thus, K does not simply represent an increase in the u_r factor of the MC. In summary, the focusing intensities simulated are basically consistent with previous research results.

Due to the hollow−core MC constraint, the magnetic flux leakage is concentrated in the square−shaped area (Figure 7). The magnetic field is reduced from a circle (d_m = 20 mm) in Figure 6 to a square (l = 12.4 mm) in Figure 7. The focusing area of the magnetic field is reduced by 160.24 mm^2. With the reduction in the focusing area, the resolution of the sensor measurement can be improved; λ is increased from 4.61 times in Figure 6 to 11.48 times in Figure 7, which realizes the focusing of magnetic flux density.

Since the magnetic field is generated via Archimedes coil excitation, no matter how the shielding is added, it does not make the total amount of magnetic field intensity increase or decrease. The original magnetic flux leakage, which is dispersed to other locations in space, is constrained along the Z−axis through the outer wall of the hollow−core MC. This function reduces the magnetic flux leakage to a negligible level, which, in turn, meets the IADSMF measurement requirement.

3.2. Induced Voltage Simulation and Linearization Analysis

Since the equation for the induced voltage is mathematically derived from this paper, simulation is used to verify the derivation. COMSOL software cannot be edited to include equations; thus, MATLAB is used for simulations to verify the equations (see Figure 8 for the simulation results). It is verified that the IADS based on magnetic focusing can realize the measurement of angular displacement through the principle of electromagnetic induction. This finding is consistent with the measurement principle described in Section 2.3.

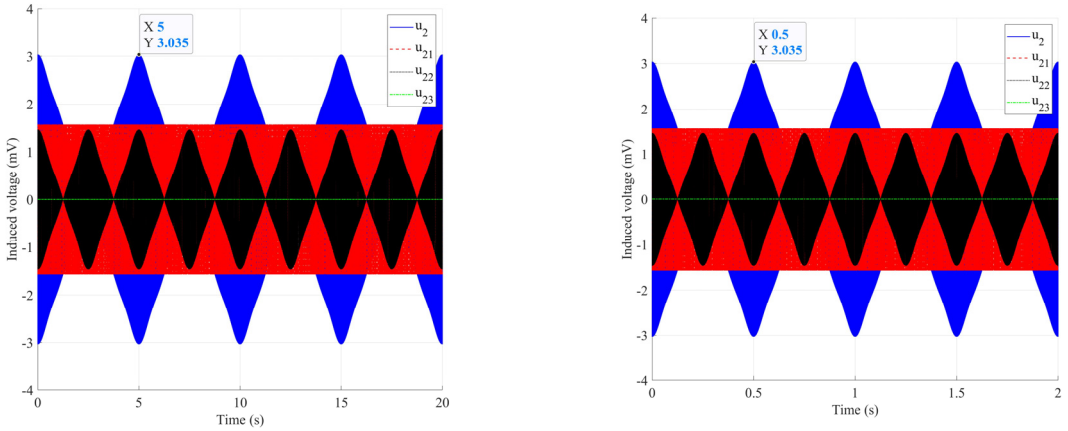

(**a**) (**b**)

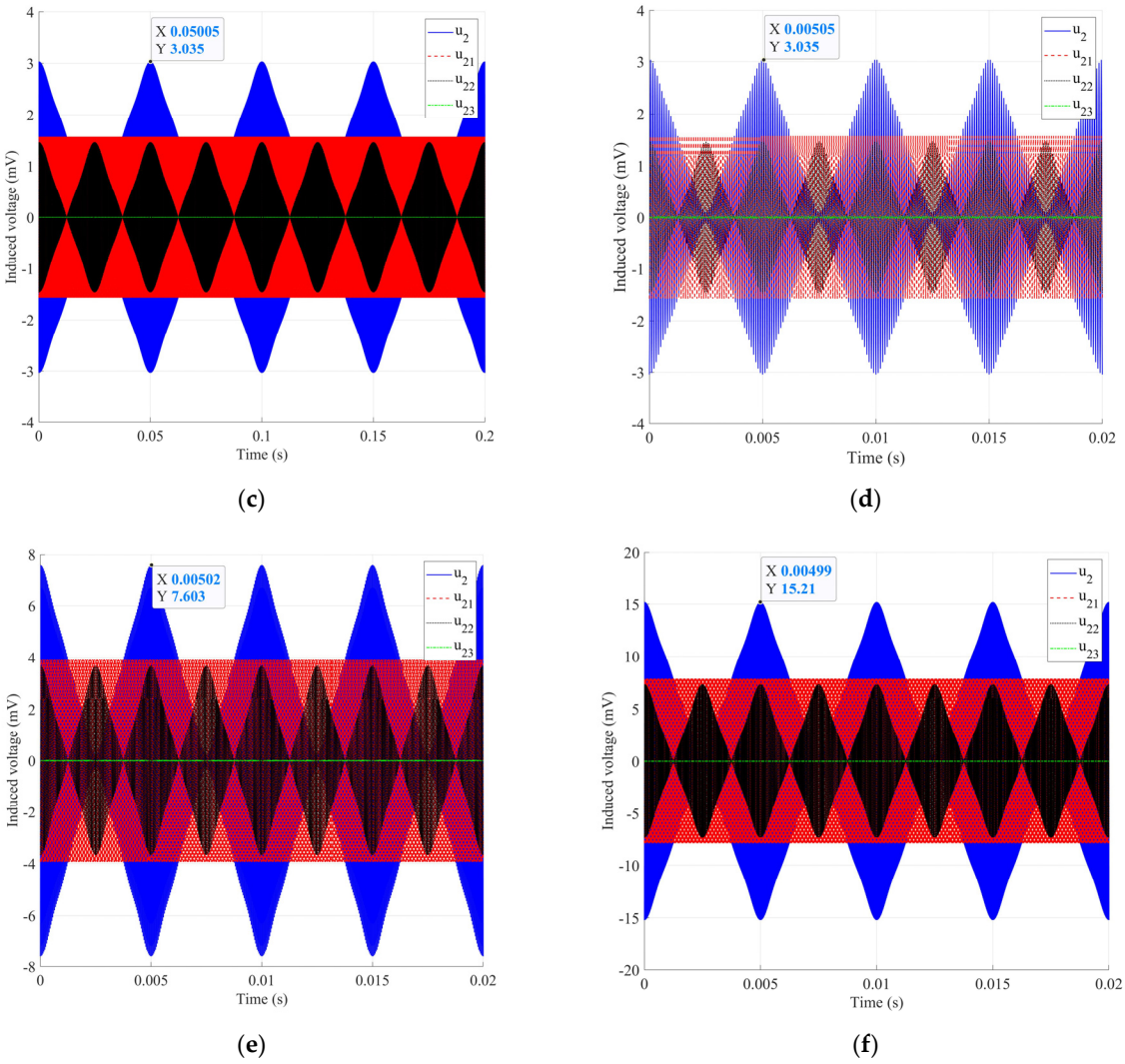

Figure 8. Simulation curves of induced voltage corresponding to different speeds and frequencies: (**a**) n_a = 1 r/min, f_1 = 10 kHz; (**b**) n_a = 10 r/min, f_1 = 10 kHz; (**c**) n_a = 100 r/min, f_1 = 10 kHz; (**d**) n_a = 1000 r/min, f_1 = 10 kHz; (**e**) n_a = 1000 r/min, f_1 = 25 kHz; and (**f**) n_a = 1000 r/min, f_1 = 50 kHz.

As can be seen in Figure 8d–f, the resolution of the IADSMF is 0.6 degrees for f_1 = 10 kHz, 0.24 degrees for f_1 = 25 kHz and 0.12 degrees for f_1 = 50 kHz. In summary, the increased resolution of the angle measurement can be achieved through simply increasing the excitation frequency while the speed is constant. The purpose of providing high angular resolution over a wide speed range is achieved.

The reason for the approximately linear relationship between time and induced voltage u_2 is that when the rotational speed n_a and excitation frequency f_1 are constant, u_2 is related only to time in Equation (21), and u_2 is a sine-like function of time. Since the amplitude of the sine function in Equation (21) is large and the independent variable time is small, u_2 is approximately linear with time (Figure 8).

The reason for the linear relationship between the angular displacement y and time is that the receiving coil and excitation magnetic field are both square−shaped. The amount of change over time is the area $S(x)$, where the receiving coil coincides with the excitation magnetic field. Since the width l in $S(x)$ (Figure 7) is constant, the overlap area is related only to the overlap length $l - |x|$ in the X−axis direction (angular displacement $y = l - |x|$). Therefore, the angular displacement is linear with time.

Since the length of time in a cycle corresponds to the spatial angular displacement, u_2 and y of the shaft assume an approximate linear relationship (Figure 5). The advantage of the proposed square−shaped receiving coil, compared with the three sets of diamond-shaped coils previously proposed [27], is that the induced voltage obtained is directly linearized, eliminating the need for an algorithm to obtain the linear relationship between the induced voltage and angle and simplifying the post−processing work. The measuring requirements can be met using a set of receiving coils designed for this purpose; thus, the receiving coil structure is simplified, and the number of wires is reduced. This outcome is the original intention of designing a square−shaped receiving coil.

When the rotational speed is constant, the induced voltage amplitude increases with increasing excitation frequency f_1 (Figure 8d–f). Here, f_1 is increased to improve the resolution and achieve more accurate and smaller angle measurements. However, if f_1 is increased excessively, electric energy will be wasted.

Advantages of IADSMF:

(1) For post−processing

There are several reasons for having different post−processing formulas (Table 5). Firstly, the sensors have different metal rotor shapes and numbers of blades. Secondly, the angle of the space occupied by its corresponding one blade is different; thus the post−processing equation is different. Moreover, each researcher has a different understanding of the sensor that they designed; thus, the defined post−processing is also different, i.e., there is no standard answer, but only the correct answer. This makes post−processing poorly versatile. Inevitably, it has caused some difficulties for researchers in understanding in the field of just−contact sensors. Since IADSMF has no metal rotor blades, there is no post−processing formula. At the same time, the focusing magnetic field is consistent with the shape of the receiving coil; thus, the direct linearization is realized.

(2) Input and output aspects

As can be seen from Table 5, in conventional IADS, the excitation frequency is generally at the MHz level in order to obtain the induced voltage at the mV level. The excitation frequency cannot be too small as, as shown in [69], f_1 = 40 kHz; if the excitation frequency is too small, the voltage cannot reach mV level. As it removes the intermediate link of the metal rotor, the advantages of IADSMF are reflected. Instead of using the eddy current magnetic field on the metal rotor to induce the output voltage, the excitation field induces the voltage directly in the receiving coils. Compared with traditional IADSs, it can reduce the sensor components and input demand of the excitation end. Its eddy current loss will also be reduced, realizing the energy saving of the sensor. The specific loss is shown in Table 6 of Section 3.3.

Table 5. Comparison of sensors.

Parameter	[27]	[64]	[69]	IADSMF
f_1	4 MHz	2 MHz	40 kHz	10 kHz
u_2 (mV)	3.25	21	1.5×10^{-6}	3.035
Post−processing formula	$U_0 = U_A$ $U_0 = U_{\bar{c}} + (U_{MAX} - U_{MIN})$ $U_0 = U_B + 3U_{MAX} - U_{MIN}$ $U_0 = U_{\bar{A}} + 5U_{MAX} - U_{MIN}$ $U_0 = U_C + 7U_{MAX} - U_{MIN}$ $U_0 = U_{\bar{B}} + 9U_{MAX} - U_{MIN}$	$\theta = \arctan\left(\frac{U_{rx1}(\theta)}{U_{rx2}(\theta)}\right)$	$\theta_p = \begin{cases} \theta_1 - \theta_2 & \text{if } (\theta_1 - \theta_2) \geq 0 \\ \theta_1 - \theta_2 + 2\pi & \text{if } (\theta_1 - \theta_2) < 0 \end{cases}$ $\theta_1, \theta_2, \theta_p \in [0, 2\pi)$	None

In the next subsection, the eddy current loss is calculated to quantify the analysis.

Table 6. Eddy current loss comparison.

Parameter	[38]	IADSMF
f_1 (kHz)	10	10
$V = a^3$ (m^3)	9.3696×10^{-10}	1.2301×10^{-8}
$\boldsymbol{B}_F$ (T)	1.2297×10^{-3}	1.4×10^{-4}
u_2 (mV)	2.934	3.035
P (W)	2.1304	0.3625

3.3. Eddy Current Loss Calculation

Since the shaft is a ferromagnetic material, there is eddy current loss; thus, it is necessary to study how to reduce the eddy current loss. While meeting measurement needs, the excitation frequency should be minimized; the lower the frequency is, the smaller the eddy current loss. Excessive eddy current also causes the shaft to heat up, and a quantity of heat is transferred to the FPC on the shaft surface. Excessive temperatures affect the stability of the FPC, resulting in unnecessary errors.

The eddy current loss [78] can be expressed via (25):

$$P = \int_v \frac{\left|\boldsymbol{J}_y\right|^2}{\gamma} \mathrm{d}V = \frac{1}{24} k_{yoke} \sigma \omega^2 \boldsymbol{B}^2 a^3 = \frac{1}{6} k_{yoke} \sigma \pi^2 f^2 \boldsymbol{B}^2 a^3, \quad (25)$$

where $\boldsymbol{B}$ and $\boldsymbol{\omega}$ represent the magnetic flux density and the angular frequency, respectively; f and a^3 represent the excitation frequency and the volume, respectively; and $k_{yoke} = 0.915$ and σ represent the correction factors for eddy current loss and the material conductivity, respectively.

The penetration depth δ of the eddy current [79] can be expressed via (26):

$$\delta = \frac{1}{\sqrt{\pi f \mu_0 \mu_r \sigma}}, \quad (26)$$

where u_0 and u_r represent the permeability of vacuum and the relative permeability, respectively; and σ is the material conductivity.

Substituting $u_0 = 4\pi \times 10^{-7}$, $u_r = 400$, $\sigma = 1 \times 10^7$ S/m, $\pi = 3.14$ and $f = 10$ kHz, we obtain $\delta = 0.08$ mm, i.e., $a_3 = 0.08$ mm. Therefore, $V_{IADSMF} = a_1 \times a_2 \times a_3 = 12.4 \times 12.4 \times 0.08 \times 10^{-9} = 1.2301 \times 10^{-8}$ m^3, and $V_{IADS} = a_1 \times a_2 \times a_3 = 58.56 \times 0.2 \times 0.08 \times 10^{-9} = 9.3696 \times 10^{-10}$ m^3.

From the conclusion of Subsection 3.1, it can be seen that the excitation frequency is reduced from 1 MHz to 10 kHz when the induced voltage is reduced by approximately 100 times. Thus, the induced voltage of [38] is reduced to 2.934 mV. At this point, the output voltage amplitudes of the IADS and IADSMF are almost equal, i.e., at the same level

of 3 mV. We calculate the eddy current loss P (Table 6). P_{IADSMF} = 0.3625 W is only 17.02% of the IADS (2.1304 W) loss. The purpose of reducing eddy current loss is achieved through replacing the eddy current field with a focusing magnetic field through the MFM.

3.4. Sensor Optimization Parameter Selection

After obtaining the linear relationship between the angular displacement and induced voltage of the sensor, the measurement error needs to be analyzed. The linearity error of the induced voltage is used to reflect the measurement error of the sensor. This error is derived from the measured induced voltage curve through fitting the difference between the measured voltage and ideal voltage at the corresponding angle. The difference is divided by the full−scale voltage to express the linearity error. L [38] can be expressed via (27):

$$L = \frac{|(u_2 - u_i)_{\max}|}{u_{FS}} \times 100\%, \quad (27)$$

where L represents the linearity error; u_2 and u_i represent the simulation voltage and the ideal voltage, respectively; and u_{FS} is the full−scale output voltage.

The main design parameters of the sensor are listed. The design parameters include the number of turns of the Archimedes coil, the width of the Archimedes coil, the air gap between the Archimedes coil and the receiving coil, and the side length of the receiving coil. The initial design parameters and ranges are shown in Table 7. The parameter that has the greatest influence on the linearity error is selected through changing the single variable. This parameter is optimized to reduce the sensor linearity error.

Table 7. Sensor model parameters.

Parameter	Initial Value	Setting Range
N_1	3	3–11
r_1 (mm)	0.2	0.2–0.4
d_g (mm)	1	0.6–1.4
lr (mm)	12.4	12.4–12.8

N_1—Archimedes coil turn number; r_1—Archimedes coil width; d_g—air gap between the Archimedes coil and receiving coil; l_r—receiving coil side length.

The initial parameters of the sensor model are used to perform the simulation. The induced voltage curve is obtained, and the linearity error is calculated (Table 8). As seen from Table 8, a corresponding simulated voltage has the maximum error (0.038 mV) with the theoretical voltage at 10°. Therefore, the maximum linearity error of the sensor in a measurement period (0–60°) is 0.6239%.

Table 8. Sensor model simulation results.

θ_r (°)	u_2 (mV)	u_i (mV)	u_2–u_i (mV)	L (%)
0	3.035	3.045	−0.01	0.1642
10	1.049	1.011	0.038	0.6239
20	−1.059	−1.023	−0.036	0.5911
30	−3.035	−3.045	0.01	0.1642
40	−1.023	−0.999	−0.024	0.3941
50	1.071	1.0353	0.0357	0.5862
60	3.035	3.045	−0.01	0.1642

θ_r—rotation angle.

3.4.1. Archimedes Coil Turn Number

Only the number of turns of the Archimedes coil is changed, and the initial values of the other design parameters remain unchanged (Table 7). The number of turns is increased from 3 to 11. The variation in the maximum and minimum linearity error is 0.0318%. The number of turns has a small effect on the linearity error of the sensor (Table 9).

Table 9. Effect of number of turns on linearity error.

N_1	r_1 (mm)	d_g (mm)	lr (mm)	L (%)	E_v (%)
3	0.2	1	12.4	0.6239	
5	0.2	1	12.4	0.6443	
7	0.2	1	12.4	0.6521	0.0318
9	0.2	1	12.4	0.6475	
11	0.2	1	12.4	0.6557	

N_1—Archimedes coil turn number; r_1–Archimedes coil width; d_g–air gap between the Archimedes coil and receiving coil; lr—receiving coil side length; E_v—error variation.

3.4.2. Archimedes Coil Width

Only the Archimedes coil width is changed, and the initial values of the other design parameters remain unchanged (Table 7). The width is increased from 0.2 to 0.4 mm. The variation in the maximum and minimum linearity error is 0.0269% (Table 10). The Archimedes coil width has a small effect on the linearity error of the sensor.

Table 10. Effect of Archimedes coil width on linearity error.

N_1	r_1 (mm)	d_g (mm)	lr (mm)	L (%)	E_v (%)
3	0.2	1	12.4	0.6239	
3	0.25	1	12.4	0.6488	
3	0.3	1	12.4	0.6479	0.0269
3	0.35	1	12.4	0.6498	
3	0.4	1	12.4	0.6508	

3.4.3. Air Gap between the Archimedes Coil and Receiving Coil

Only the air gap between the Archimedes coil and receiving coil is changed, and the initial values of the other design parameters remain unchanged (Table 7). The air gap is increased from 0.6 to 1.4 mm. The variation in the maximum and minimum linearity error is 0.6219% (Table 11). The air gap has a significant effect on the linearity error of the sensor.

Table 11. Effect of air gap on linearity error.

N_1	r_1 (mm)	d_g (mm)	lr (mm)	L (%)	E_v (%)
3	0.2	0.6	12.4	0.7389	
3	0.2	0.8	12.4	0.6663	
3	0.2	1	12.4	0.6239	0.6219
3	0.2	1.2	12.4	0.8043	
3	0.2	1.4	12.4	1.2458	

3.4.4. Receiving Coil Side Length

Only the receiving coil side length is changed, and the initial values of the other design parameters remain unchanged (Table 7). The side length is increased from 12.4 to 12.8 mm. The variation in the maximum and minimum linearity error is 0.0305% (Table 12). The side length has a small effect on the linearity error of the sensor.

Table 12. Effect of side length on linearity error.

N_1	r_1 (mm)	d_g (mm)	lr (mm)	L (%)	E_v (%)
3	0.2	1	12.4	0.6239	
5	0.2	1	12.5	0.6533	
7	0.2	1	12.6	0.6399	0.0305
9	0.2	1	12.7	0.6485	
11	0.2	1	12.8	0.6544	

3.4.5. Optimization Parameter Selection

The magnitude of the error variation indicates the magnitude of the voltage fluctuation. We calculate the magnitude of error variation in the Archimedes coil turn number, Archimedes coil width, air gap between the Archimedes coil and the receiving coil, and receiving coil side length. The maximum error variation for each parameter is shown in Table 13. From these, the parameter corresponding to the maximum error variation is selected and optimized.

Table 13. Effect of the main design parameters on E_v.

Parameter	E_v (%)
N_1	0.0318
r_1 (mm)	0.0269
d_g (mm)	0.6219
l_r (mm)	0.0305

When the distance of the air gap is changed from 0.6 to 1.4 mm, the magnitude of the error variation is 0.6219% (Table 13). E_v of the air gap is an order of magnitude larger than that of the other parameters. The air gap is a main parameter affecting the linearity error of the sensor. Therefore, the air gap is selected as an optimized parameter for the sensor.

3.5. Optimization Algorithm

Nowadays, the algorithm is being developed very rapidly, and new algorithms are everywhere. For example, the IbI Logics Algorithm (ILA) is based on Intelligible-in-time (IbI) Logics [80]. Its advantage over existing algorithms is that the optimization can be divided into three phases, which can be optimized in stages. If there is a problem in the second stage, the third stage will not be executed. Correct the problems in the second phase before implementing the next phase. It is suitable for scenarios where the entire optimization process needs to be monitored and the optimization parameters need to be continuously improved (e.g., changing the number of iterations). There is also an optimization algorithm applied to exoplanet exploration–Transit Search (TS) [81]. For the optimization approach used through TS, different optimization strategies are used at different stages of optimization. It optimizes 73 constraints, and the total average error of TS is the lowest compared with the existing algorithms. Therefore, it is suitable for outer space exoplanet exploration. The algorithm is suitable for multi−constrained problems, and its effect of equilibrium is good.

In recent years, researchers optimized sensor structures or related parameters through various optimization algorithms. The algorithms used are surface integral method [82], particle swarm optimization (PSO) [83] and response surface method [38]. PSO is suitable for solving global optimization problems. Compared with traditional algorithms, PSO has fast solving speed and guarantees global search ability [84]. However, PSO has the problem of premature convergence and may converge at the local optimum solution. Considering the above shortcomings, Jing et al. improved the PSO via adding inertia weights to the PSO. The inertia weights can decrease non−linearly with the number

of iterations increasing. Thus, it ensures global search capability while avoiding trapping searches in local optimal solutions [85].

Linearly decreasing inertia weight particle swarm optimization (LIWPSO) and the finite element method (FEM) are combined to optimize the sensor parameters. The sensor parameter design problem is transformed into a particle swarm search for the best position. LIWPSO has two key factors for the position search: (1) particle velocity ($v_{i,j}$) and (2) particle position ($x_{i,j}$) [27]. The particle velocity represents the magnitude of the ability to find a solution. In the n−dimensional search space, each position of a particle represents a solution to the fitness function, i.e., a position corresponds to a set of sensor structure parameters. LIWPSO finds the optimal structure variable through solving for the optimal value of the fitness function in the search space. Using the above variable, the corresponding parameters are changed, and the sensor is simulated via the FEM.

Linearity error is calculated through comparing the simulated voltage profile with the ideal voltage profile, i.e., LIWPSO finds a set of structural parameters that minimize the sensor linearity error. The updated formulas [27] of the LIWPSO particle velocity and position can be obtained via (28) and (29), respectively:

$$v_{i,j}(t+1) = \omega v_{i,j}(t) + c_1 r_1(t)(p_{i,j}(t) - x_{i,j}(t)) + c_2 r_2(t)(g_{i,j}(t) - x_{i,j}(t)), \quad (28)$$

$$x_{i,j}(t+1) = x_{i,j}(t) + v_{i,j}(t), \quad (29)$$

where $v_{i,j}$ represents the particle velocity; ω represents the inertia weight; $x_{i,j}$ represents the particle position; c_1 and c_2 represent the acceleration coefficients of individual particles and the particle swarm, respectively; and r_1 and r_2 represent random numbers uniformly distributed on the interval [0, 1].

The inertia weight formula [27] can be obtained via (30):

$$\omega = \omega_{\max} + \frac{t \cdot (\omega_{\min} - \omega_{\max})}{t_{\max}}, \quad (30)$$

where ω_{max} represents the maximum inertia weight, ω_{min} is the minimum inertia weight and t_{max} is the maximum number of iterative steps.

In LIWPSO, $\boldsymbol{\omega}$ should be maintained at a large value at the beginning to ensure that particles jump out of the local optimal solution. Additionally, $\boldsymbol{\omega}$ should be maintained at a small value when the number of iterations is large to ensure that this parameter tends to the global optimal solution and facilitate algorithm convergence. Generally, $\boldsymbol{\omega}_{min} = 0.4$, and $\boldsymbol{\omega}_{max} = 0.9$. Figure 9 shows the LINWPSO optimization process.

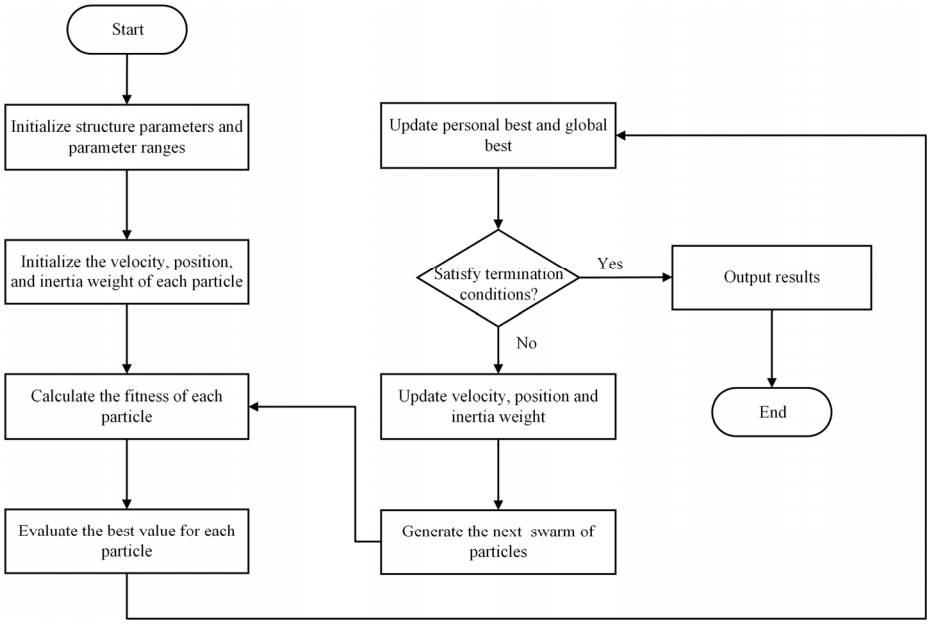

Figure 9. Flow chart of LINWPSO optimization process.

In LIWPSO–FEM, the fitness function is used to represent the sensor linearity error. The air gap between the Archimedes coil and receiving coil is used as the optimized parameter. The optimization design of the sensor is transformed into the problem of determining the values of the sensor variables through searching for the minimum fitness function via LIWPSO–FEM [27]. The fitness function [38] can be expressed via (31):

$$fitness = L = \frac{|(u_2 - u_i)_{\max}|}{u_{\mathrm{FS}}} \times 100\%, \quad (31)$$

where L is the sensor linearity error; u_2 and u_i represent the simulated voltage and the ideal voltage, respectively; and u_{FS} is the full–scale output voltage.

In the optimization process of LIWPSO–FEM, the particle swarm size is 120, the acceleration coefficients $c_1 = c_2 = 1.495$ and $-0.05 \le v_{i,j} \le 0.05$. The number of iterations is 30. The minimum fitness, i.e., the linearity error value, is obtained through 30 iterations. The linearity error is stable at 0.6012% when the number of iterations exceeds 11 (Figure 10a). The variation range of the air gap is 0.6–1.4 mm, and the air gap distance corresponding to the minimum linearity error is 0.96 mm (Figure 10b).

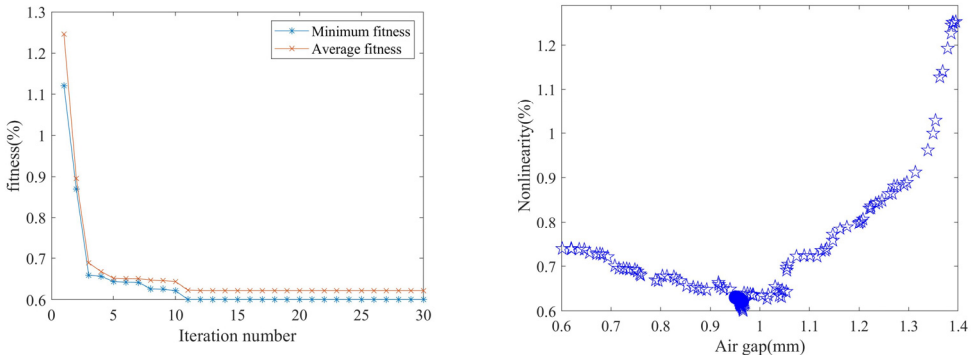

(**a**) (**b**)

Figure 10. Sensor optimization simulations: (**a**) fitness value with iteration number; (**b**) linearity error vs. the air gap obtained in optimization design.

The optimized linearity error, as shown in Table 14.

Table 14. Linearity error corresponding to optimized sensor parameter.

Parameter	*L* (%)
d_g = 0.96 (mm)	0.6012

In Table 15, a comparative study is given for the IADSMF and some inductive displacement sensors. After optimization, the proposed IADSMF has a lower linearity error. The advantage of direct linearization is, thus, demonstrated.

Table 15. Linearity comparison of IADSMF and other displacement sensors.

Sensor	*L* (%)
[27]	0.778
[86]	0.8
[87]	1.25
IADSMF	0.6012

4. Discussion

The achievements and shortcomings are as follows.

The main engines of large ships usually operate at low−to−medium speeds. Therefore, the main engine speed is usually in the range of 90–120 r/min [88]. As shown in Figure 8c, n_a = 100 r/min, and the angular resolution is 0.06 degrees. The resolution of IADSMF is higher than shown in [89,15] (0.5 and 0.35 degrees). Higher or lower angular resolution can be achieved through changing f_1.

In contrast to crankshaft angle measurement using an optical angle encoder set, the IADSMF does not require a separate electronic module for converting the optical signal into standard TTL signal [89]. IADSMF reduces the complexity of sensors.

Magnetic focusing is used as the excitation method to reduce one level of transmission compared with a traditional IADS. A traditional IADS [27,36–38] is composed of three parts—excitation, rotor and receiving coils—requiring two-level transmission to complete a measurement. The working mode occurs as follows: (1) the excitation coil produces a magnetic field due to rotor rotation, and an eddy current is created in the rotor. The rotor undergoes a position change relative to the receiving coil; (2) the receiving coil then induces a voltage through the eddy current magnetic field generated using the rotor to achieve the position measurement. An IADSMF forms a stator through means of the MC and the excitation coil. The generated focusing magnetic field directly acts on the FPC receiving coil on the rotor, and the FPC receiving coil directly induces a voltage.

The focusing magnetic field from the excitation end replaces the eddy current magnetic field of the IADS. The eddy current magnetic field inside the metal rotor is eliminated, again avoiding inducing a voltage at the receiving coil end. Thus, the eddy current field can be reduced, and the purpose of reducing eddy current loss can be achieved (Table 6).

The excitation frequency is 10 kHz for IADSMF and 4 MHz for [27], and the induced voltage amplitude of the two sensors are 3 mV. Therefore, when this sensor outputs the same magnitude of induced voltage as the previously studied sensor [27], there is no need for a MHz−level excitation frequency. The reason for this finding is that the introduction of magnetic focusing increases the magnetic induction intensity acting directly on the receiving end.

In terms of linearization, the focusing magnetic field and the receiving coil of the IADSMF are square−shaped to achieve direct linearization. The linearity error of the IADSMF before optimization is 0.6239% (0.6012% after optimization), which is less than the linearity error of a traditional IADS, which is optimized to 0.778% [27].

The sensitivity of the IADSMF is 0.2023 mV/°, while the sensor sensitivity shown in [27] is 0.4847 mV/°; the IADSMF value is lower. The definition of sensitivity shows that the higher the sensitivity, the narrower the measurement range of angular displacement, and the lower the sensor's stability. Although the IADSMF sensitivity is low, its stability is better than that of [27].

In terms of the angle measurement range, the IADSMF can achieve 0–360° measurement without the constraint associated with the measuring angle range. However, in [37], it does not calculate the angle corresponding to the induced voltage of 0 mV, and there is a defect in the range of angle measurement. The advantage of direct linearization is further demonstrated.

In terms of the optimization algorithm, LINWPSO has a strong ability to jump out of local optimal solutions. LINWPSO has a faster calculation speed and shorter calculation time than the traditional particle swarm optimization method used in [37].

The MFM is used to change the traditional excitation method, and a breakthrough in the excitation method of an IADS is realized. The above breakthrough and improvements enabled the direct linearization of angular displacement and induced voltage, thus reducing post−processing design and calculation.

The following issues should be the focus of future research.

The focus of future research is a comprehensive study of signal transmission at the sensor output. The induced voltage would be sent to the host computer through a wireless transmission technology such as Bluetooth. Among them, electromagnetic interference and miniaturization of transmission devices are the focus of research.

(1) Electromagnetic interference

Through debugging different excitation and transmission frequencies, we would discover a suitable electromagnetic compatibility scheme. The effect of different directions for the transmitted signal on the excitation would be sought in space. We would aim to find the best decoupling scheme for the transmission signal and the excitation signal or the scheme with the least influence [90].

(2) Miniaturization aspect

We would use manufacturing technologies, such as inkjet printing or silicon micromachining technologies, to manufacture circuit boards. We would use these technologies to take advantage of their smaller size and ability to arrange multi−layer coils on a very small area, as well as their amplifiers, low-pass filters, analog−to−digital converters, Bluetooth transceivers, and other components to create transmission devices [91–93].

5. Conclusions

Based on the advantages of IADS, a magnetic focusing type sensor suitable for using in the environment of ships is designed. The sensor has good versatility and scalability. An IADSMF can realize the measurement of the crankshaft angle position. Two IADSMFs are combined to enable the measurement of torque on ships' rotating shafts. Compared to the optical method of torque measurement, the IADSMF does not require an additional geared system for torque measurement. Therefore, the machining of the shaft is simplified. Compared to traditional IADS, IADSMF does not require a metal rotor in either a planar or vertical structure. This fact results in one less component being in the overall sensor system. The purpose of creating a simpler system and higher reliability in the engineering application is realized. In addition, IADSMF is a non−contact sensor; thus, there is no need to worry about contact friction and service life.

Compared to the resolution of existing crankshaft angle encoders (0.35 and 0.5 degrees), the IADSMF increases the measurement resolution (0.06 degrees) by a factor of 5.8 to 8.3. If necessary, the resolution improvement could be achieved through increasing the existing excitation frequency (10 kHz). The increase in excitation frequency would be proportional to the increase in resolution (Figure 8d–f).

Through combining an Archimedes coil with a hollow−core MC, the magnetic field generated using the excitation coil is changed from a circular (d_m = 20 mm) to an approximately square−shaped magnetic field (12.4 × 12.4 mm^2). This method reduces the magnetic field's area by 51.03%. It improves the center−focusing degree and sensor resolution and realizes magnetic field focusing. The stator is composed of metal MCs and Archimedes coils. The rotor is composed of a set of 12 square−shaped receiving coils connected at the beginning and end, with the adjacent receiving coils separated by 15°. A measurement cycle is 60°, and the angular displacement measurement of rotating in a circle can be completed in six measurement cycles.

Mathematical models of the excitation coil magnetic field, the receiving coil area change and the induced voltage are derived. Subsequent simulations are performed for rotational speeds from 1 to 1000 r/min. The simulation results show that the relationship between the shaft angular displacement information and induced voltage of the receiving coil is approximately sinusoidal. The reason for the linearization of angular displacement with respect to the induced voltage is analyzed, being achieved using the square−shaped magnetic field and receiving coil design. Theoretically, the feasibility of the measurement principle of this sensor is demonstrated, and the direct linearization of the angular displacement and induced voltage is achieved. The IADSMF corresponds to an initial linearity error of 0.6239%. As can be seen from the data in Table 15, this error is also smaller than that of the other IADSs. The above finding shows that it is beneficial to the proposed direct linearization, while its effect is good. Simplifying the post−processing design reduces the difficulty of sensor development and avoids the calculation error that IADS may cause due to subsequent complex linearization calculation. According to equations and simulations, it is concluded that excitation frequency f_1 is the main factor affecting the induced voltage amplitude. The amplitude of u_2 increases proportionally with increasing f_1. At f_1 = 10 kHz, the influence of a low rotational speed change on the amplitude of u_2 can be ignored. The eddy current loss of a traditional IADS is 2.1304 W, while that of the IADSMF is 0.3625 W for almost the same induced voltage amplitude, achieving a reduction in the eddy current loss. The above eddy current loss calculation shows that the measurement method adopted using IADSMF changes the original IADS, which requires a large eddy current magnetic field to implement the angle measurement. A shortcoming in the design of IADS is solved, i.e., the eddy current field of IADS cannot be too small, otherwise the induced voltage cannot reach the mV level to achieve measurement. Moreover, an excessive eddy current field corresponds to a large eddy current loss, which is not conducive to the energy saving of the sensor. Therefore, IADSMF provides a research idea for the development of IADS family. The parameter that has the greatest influence on the linearity error of the IADSMF—the air gap—is identified through simulations. The sensor structure is then optimized via LIWPSO to find the minimum linearity error of 0.6012%, corresponding to an air gap of 0.96 mm.

During optimization, the change in air gap affects the focusing effect of magnetic field, which, in turn, affects the linearity. Thus, it is found that the better the focusing effect of magnetic field, the less the magnetic flux leakage outside the receiving coil of IADSMF, and the less it affects the measurement results. Therefore, future research can improve the focusing effect. For example, we could find a material with greater relative magnetic permeability than hollow−core MC to further constrain magnetic flux leakage. Moreover, different materials of solid−core MC are selected and combined with hollow−core MC. We could also find the best combination of hollow− and solid−core MC to improve the focusing effect. The introduction of MFM into IADS further advanced application of MFM in the measurement field. In particular, one potential application is angle measurement in ships, which is based on the advantages of direct linearization of IADSMF, which, in turn, contributed to the advancement in reducing the design difficulty and understanding aspect of IADS. As shown in Table 5, there is no need for designers to convert angles or voltages. For researchers who are not experts in the field of sensors, it is not necessary to

understand the design principles and formulas of each sensor post−processing. The linearity of the voltage variation with time (angular displacement) can be visualized. The versatility and readability of IADS in post−processing are improved.

Since the IADSMF does not have a metal rotor, we allow the IADS to bypass the eddy current magnetic field. The excitation magnetic field is realized via inducing a voltage directly into the receiving coil. The improvement of measurement method is realized. For the designer, it avoids a situation in which the sensor, knowing that the greater the eddy current, the greater the loss (Table 6), cannot reduce the eddy current significantly. Otherwise, the induced voltage amplitude is too small to be measured, making the IADS useless as a sensor.

In ships, the cost of developing a separate torque sensor is five times that of an angle sensor [15]. While using IADSMF to replace the angle encoder of the ship main engine, there is no need to separately develop a torque sensor applied to the ship. Instead, we can simply place another IADSMF on the other end of the shaft. Through measuring the torsion angle between two IADSMFs, the torque can be measured using the formula, improving versatility and reducing costs. A potential application area for the IADSMF is torque measurement on ships. This function promotes the measurement and application of magnetic focusing knowledge in the field of torque.

An inductive sensor and the MFM are combined to realize the breakthrough of the IADS measurement method in theory. This method provides a theoretical basis and new research directions to promote further IADS development in ships and navigation. We will experiment with the application of IADSMF in ships and navigation in our next steps.

Experimental arrangement:

(1) According to the data in Table 3, the solid− and hollow−core MCs are processed, and they are combined with the PCB containing the Archimedes coil.
(2) Using a Gauss meter, we measured the magnetic field formed using the MFM proposed in Section 3.1 to verify that the focus was successful.
(3) According to the actual focused square magnetic field, the FPC receiving coil with the same size was processed.
(4) We processed the shaft, purchase and manufacture equipment, such as the drive motor, frequency inverter, excitation power supply, couplings and transmission equipment.
(5) After the sensor assembly was completed, the sensor was tested and calibrated to determine the measurement angle, the linearity error and repeatability, etc.

After the above experiments were completed, IADSMF was installed on the free end of the crankshaft of the main engine for board testing.

6. Patents

Li, Z.; Wang, B.; Guo, Y.; Zhang, C.; Qiu, F. A measurement system based on magnetic focusing type to measure static torque and its measurement method. CN110987259B, 30 November 2021.

Li, Z.; Zhang, C.; Qiu, F.; Wang, B.; Meng, X. A dual magnetic focusing speed, torque and angle sensor. CN210486909U, 8 May 2020.

Author Contributions: Conceptualization, Z.L. and B.W.; methodology, Z.L. and B.W.; software, B.W. and X.W; validation, Z.L., B.W. and X.W.; formal analysis, X.M. and C.Z.; investigation, B.W.; resources, and C.Z.; data curation, B.W.; writing—original draft preparation, B.W.; writing—review and editing, Z.L.; supervision, Z.L.; project administration, Z.L.; funding acquisition, Z.L. All authors have read and agreed to the published version of the manuscript.

Funding: This research was funded by the National Natural Science Foundation of China, funding number 52175497, and the Key R&D Program of Heilongjiang Province in China, funding number JD22A014.

Institutional Review Board Statement: Not applicable.

Informed Consent Statement: Not applicable.

Data Availability Statement: Not applicable.

Acknowledgments: The authors would like to express their sincere thanks to all of the members of the research team for their contributions to this research. The authors are also grateful in advance to the reviewers and editors for their comments and suggestions on how to improve the manuscript.

Conflicts of Interest: The authors declare no conflicts of interest.

References

1. Chung, W.C.; Jin, C.; Kim, M. Dual-algorithm hybrid method for riser structural health monitoring using the fewest sensors. *J. Mar. Sci. Eng.* **2022**, *10*, 1994. https://doi.org/10.3390/jmse10121994.
2. Kim, H.; Jin, C.; Kim, M. Real-time estimation of riser's deformed shape using inclinometers and extended Kalman filter. *Mar. Struct.* **2021**, *77*, 102933. https://doi.org/10.1016/j.marstruc.2021.102933.
3. Suzuki, R.; Tsukada, Y.; Ueno, M. Estimation of full-scale ship manoeuvrability in adverse weather using free-running model test. *Ocean Eng.* **2020**, *213*, 107562. https://doi.org/10.1016/j.oceaneng.2020.107562.
4. Zhang, X.X.; Shan, X.B.; Xie, T.; Miao, J.M.; Du, H.J.; Song, R.J.; Harbor seal whisker inspired self-powered piezoelectric sensor for detecting the underwater flow angle of attack and velocity. *Measurement* **2021**, *172*, 108866. https://doi.org/10.1016/j.measurement.2020.108866.
5. Zheng, J.; Chen, J.; Wu, X.; Liang, H.; Zheng, Z.; Zhu, C.; Liu, Y.; Sun, C.; Wang, C.; He, D. Analysis and compensation of installation perpendicularity error in unmanned surface vehicle electro-optical devices by using sea-sky line images. *J. Mar. Sci. Eng.* **2023**, *11*, 863. https://doi.org/10.3390/jmse11040863.
6. Hu, P.; Cui, Y.; Zhao, C.; Li, Y.; Li, B. Numerical investigation on the hydrodynamic response of pentamaran-resistance analysis of different outrigger inclination angles. *J. Mar. Sci. Eng.* **2023**, *11*, 186. https://doi.org/10.3390/jmse11010186.
7. Lee, D.; Ku, N.; Kim, T.W.; Kim, J.; Lee, K.Y.; Son, Y.S. Development and application of an intelligent welding robot system for shipbuilding. *Robot. Comput. Integr. Manuf.* **2011**, *27*, 377–388. https://doi.org/10.1016/j.rcim.2010.08.006.
8. Chen, S.F.; Liu, J.; Chen, B.; Suo, X.Y. Universal fillet weld joint recognition and positioning for robot welding using structured light. *Robot. Comput. Integr. Manuf.* **2022**, *74*, 102279. https://doi.org/10.1016/j.rcim.2021.102279.
9. Wu, W.; Chen, S.; Qin, S. Online estimation of ship dynamic flexure model parameters for transfer alignment. *IEEE Trans. Control Syst. Technol.* **2013**, *21*, 1666–1678. https://doi.org/10.1109/TCST.2012.2214778.
10. Hasanvand, A.; Hajivand, A.; Ali, N.A. Investigating the effect of rudder profile on 6DOF ship turning performance. *Appl. Ocean Res.* **2019**, *92*, 101918. https://doi.org/10.1016/j.apor.2019.101918.
11. Zhou, R.; Chen, J.; Tan, W.; Cai, C. Sensor selection for optimal target localization with 3-D angle of arrival estimation in underwater wireless sensor networks. *J. Mar. Sci. Eng.* **2022**, *10*, 245. https://doi.org/10.3390/jmse10020245.
12. Ullah, I.; Chen, J.; Su, X.; Esposito, C.; Choi, C. Localization and detection of targets in underwater wireless sensor using distance and angle based algorithms. *IEEE Access* **2019**, *7*, 45693–45704. https://doi.org/10.1109/ACCESS.2019.2909133.
13. Wang, P.; Tian, X.L.; Peng, T.; Luo, Y. A review of the state-of-the-art developments in the field monitoring of offshore structures. *Ocean Eng.* **2018**, *147*, 148–164. https://doi.org/10.1016/j.oceaneng.2017.10.014.
14. Mentjes, J.; Wiards, H.; Feuerstack, S. Berthing assistant system using reference points. *J. Mar. Sci. Eng.* **2022**, *10*, 385. https://doi.org/10.3390/jmse10030385.
15. Jiménez Espadafor, F.J.; Becerra Villanueva, J.A.; Guerrero, D.P.; García, M.T.; Trujillo, E.C.; Vacas, F.F. Measurement and analysis of instantaneous torque and angular velocity variations of a low speed two stroke diesel engine. *Mech. Syst. Signal. Process.* **2014**, *49*, 135–153. https://doi.org/10.1016/j.ymssp.2014.04.016.
16. Doan, M.N.; Kai, Y.; Obi, S. Twin marine hydrokinetic cross-flow turbines in counter rotating configurations: A laboratory-scaled apparatus for power measurement. *J. Mar. Sci. Eng.* **2020**, *8*, 918. https://doi.org/10.3390/jmse8110918.
17. Li, Z.P.; Wang, B.N.; Meng, X.; Zhang, C. Principle, study status and development trend of the electromagnetic torque sensor. *Chin. J. Sci. Instrum.* **2021**, *42*, 1–14. https://doi.org/10.19650/j.cnki.cjsi.J2007154.
18. Dudojc, B.; Mindykowski, J. New approach to analysis of selected measurement and monitoring systems solutions in ship technology. *Sensors* **2019**, *19*, 1775. https://doi.org/10.3390/s19081775.
19. Mohankumar, P.; Ajayan, J.; Yasodharan, R.; Devendran, P.; Sambasivam, R. A review of micromachined sensors for automotive applications. *Measurement* **2019**, *140*, 305–322. https://doi.org/10.1016/j.measurement.2019.03.064.
20. Noguchi, A.; Yamawaki, K.; Yamamoto, T.; Toratani, T. Development of a steering angle and torque sensor of contact-type. *Furukawa Rev* **2004**, *25*, 36–41.
21. Lee, K.T.; Chee, P.S.; Lim, E.H.; Kam, Y.H. Data glove with integrated Polyethylene-Carbon Composite-Based strain sensor for virtual reality applications. *Chem. Eng. Technol.* **2023**, *46*, 1–8. https://doi.org/10.1002/ceat.202200569.
22. Fu, Y.C.; Fan, W.; Jin, H.X.; Chen, Q. A new capacitance angle sensor of concentric ring multi-layer differential. *Measurement* **2020**, *158*, 107625. https://doi.org/10.1016/j.measurement.2020.107625.
23. Wu, J.; Meng, Z.; Zhang, X.; Mi, W.; Yan, Y. Capacitive angle sensor research using COMSOL Multiphysics. *Appl. Sci.* **2023**, *13*, 2937. https://doi.org/10.3390/app13052937.

24. Sreevidya, P.V.; Borole, U.P.; Kadam, R.; Khan, J.; Barshilia, H.C.; Chowdhury, P. A novel AMR based angle sensor with reduced harmonic errors for automotive applications. *Sens. Actuators A Phys.* **2021**, *324*, 112573. https://doi.org/10.1016/j.sna.2021.112573.
25. Cubells-beltrán, M.D.; Reig, C.; Madrenas, J.; Marcellis, A.D.; Santos, J.; Cardoso, S.; Freitas, P.P. Integration of GMR sensors with different technologies. *Sensors* **2016**, *16*, 939. https://doi.org/10.3390/s16060939.
26. Wang, Y.Y.; Qin, Y.; Chen, X.H.; Peng, D.L.; Tang, Q.F.; Zhang, T.H. Angular displacement sensor for gear position detection based on the tunneling magnetoresistance effect. *Meas. Sci. Technol.* **2023**, *34*, 025112. https://doi.org/10.1088/1361-6501/aca0b0.
27. Li, Z.P.; Zhang, C.; Shi, S.Z.; Meng, X.; Wang, B.N. Design and parameter optimization of contactless vertical inductive angle sensor. *Vacuum* **2019**, *169*, 108865. https://doi.org/10.1016/j.vacuum.2019.108865.
28. Li, Y.; Li, R.; Yang, J.; Xu, J.; Yu, X. Effect of excitation signal on double-coil inductive displacement transducer. *Sensors* **2023**, *23*, 3780. https://doi.org/10.3390/s23073780.
29. Hou, H.; Cao, G.H.; Ding, H.C.; Li, K. Research on particle swarm compensation method for subdivision error optimization of photoelectric encoder based on parallel iteration. *Sensors* **2022**, *22*, 4456. https://doi.org/10.3390/s22124456.
30. Wang, X.J. Errors and precision analysis of subdivision signals for photoelectric angle encoders. *Opt. Precis. Eng.* **2012**, *20*, 379–386. https://doi.org/10.3788/OPE.20122002.0379.
31. Tan, N.Y.J.; Liu, K.; Senthil Kumar, A. Multiple axis ultra-precision freeform deviation control using encoder data analysis. *J. Manuf. Process.* **2023**, *90*, 242–256. https://doi.org/10.1016/j.jmapro.2023.01.079.
32. Das, S.; Chakraborty, B. Design and realization of an optical rotary sensor. *IEEE Sens. J* **2018**, *18*, 2675–2681. https://doi.org/10.1109/JSEN.2018.2794822.
33. Agarwal, S.; Shakher, C. In-plane displacement measurement by using circular grating Talbot interferometer. *Opt. Lasers Eng.* **2015**, *75*, 63–71. https://doi.org/10.1016/lj.optlaseng.2015.06.011.
34. Guerrero-Mendez, C.D.; Arco, L.D.; Pontes, M.J.; Segatto, M.E.V.; Cifuentes, C.A.; Bastos-Filho, T.F.; Diaz, C.A.R. Fatigue test on optical fiber angle sensors based on polymeric materials for flexion–extension applications. *Opt. Fiber Technol.* **2023**, *78*, 103334. https://doi.org/10.1016/j.yofte.2023.103334.
35. Twu, R.C.; Lin, B.L. Development and investigation of birefringent Beta-Barium borate for optical angle sensor. *Opt. Laser Technol.* **2022**, *155*, 108369. https://doi.org/10.1016/j.optlastec.2022.108369.
36. Dauth, R.A.; Gerlach, G.; Fella, S. An effective method to model and simulate the behavior of inductive angle encoders. *Sensors* **2022**, *22*, 7804. https://doi.org/10.3390/s22207804.
37. Ye, L.; Yang, M.; Xu, L.; Zhuang, X.Q.; Dong, Z.P.; Li, S.Y. Nonlinearity analysis and parameters optimization for inductive angle sensor. *Sensors* **2014**, *14*, 4111–4125. https://doi.org/10.3390/s140304111.
38. Ye, L.; Yang, M.; Xu, L.; Guo, C.; Li, L.; Wang, D.Q. Optimization of inductive angle sensor using response surface methodology and finite element method. *Measurement* **2014**, *48*, 252–262. https://doi.org/10.1016/j.measurement.2013.11.017.
39. Jia, H.Z. Current status of electron beam selective melting additive manufacturing technology. *J. Phys. Conf. Ser.* **2021**, *2044*, 012126. https://doi.org/10.1088/1742-6596/2044/1/012126.
40. Hartog, S.D.; Neukermans, S.; Samanipour, M.; Vincent Ching, H.Y.; Breugelmans, T.; Hubin, A.; Ustarroz, J. Electrocatalysis under a magnetic lens: A combined electrochemistry and electron paramagnetic resonance review. *Electrochim. Acta* **2022**, *407*, 139704. https://doi.org/10.1016/j.electacta.2021.139704.
41. Zhang, L.P.; Chang, L.; Yuan, X.G.; Zhang, J.H.; Zhou, H.S.;Luo, G.N. A RF plasma source with focused magnetic field for material treatment. *Plasma Chem. Plasma Process.* **2023**, *43*, 329–345. https://doi.org/10.1007/s11090-022-10300-z.
42. Konečná, A.; Javier García de Abajo, F. Electron beam aberration correction using optical near fields. *Phys. Rev. Lett.* **2020**, *125*, 030801. https://doi.org/10.1103/PhysRevLett.125.030801.
43. Grillo, V.; Tavabi, A.H.; Yucelen, E.; Lu, P.H.; Venturi, F.; Larocque, H.; Jin, L.; Savenko, A.; Gazzadi, G.C.; Balboni, R.; et al. Towards a holographic approach to spherical aberration correction in scanning transmission electron microscopy. *Opt. Express* **2017**, *25*, 21851–21860. https://doi.org/10.48550/arXiv.1705.04903.
44. Siegbahn, K.; Svartholm, N. Focusing of electrons in two dimensions by an inhomogeneous magnetic field. *Nature* **1946**, *157*, 872–873. https://doi.org/10.1038/157872b0.
45. Walton, E.T.S. High-order focusing by a uniform magnetic field with straight-line boundaries. *Nature* **1954**, *173*, 1147–1148. https://doi.org/10.1038/1731147a0.
46. Damadian, R.; Minkoff, L.; Goldsmith, M.; Stanford, M.; Koutcher, J. Field focusing nuclear magnetic resonance (FONAR): Visualization of a tumor in a live animal. *Science* **1976**, *194*, 1430–1432. https://doi.org/10.1126/science.1006309.
47. Lefaucheur JP. Transcranial magnetic stimulation. Handb Clin Neurol. 2019, 160, 559-580. DOI: 10.1016/B978-0-444-64032-1.00037-0.
48. Mazurek, M.H.; Cahn, B.A.; Yuen, M.M.; Prabhat, A.M.; Chavva, I.R.; Shah, J.T.; Crawford, A.L.; Brian-welch, E.; Rothberg, J.; Sacolick, L.; et al. Portable, bedside, low-field magnetic resonance imaging for evaluation of intracerebral hemorrhage. *Nat. Commun.* **2021**, *12*, 5119. https://doi.org/10.1038/s41467-021-25441-6.
49. Kee, H.; Lee, H.; Park, S. Optimized Halbach array for focused magnetic drug targeting. *J. Magn. Magn. Mater.* **2020**, *514*, 167180. https://doi.org/10.1016/j.jmmm.2020.167180.
50. Liu, Y.L.; Chen, D.; Shang, P.; Yin, D.C. A review of magnet systems for targeted drug delivery. *J. Control. Release* **2019**, *302*, 90–104. https://doi.org/10.1016/j.jconrel.2019.03.031.
51. Alexiou, C.; Diehl, D.; Henninger, P.; Iro, H.; Rockelein, R.; Schmidt, W.; Weber, H. A high field gradient magnet for magnetic drug targeting. *IEEE Trans. Appl. Supercond.* **2006**, *16*, 1527–1530. https://doi.org/10.1109/TASC.2005.864457.

52. Zhao, Y.Z.; Wang, X.H.; Sun, T.; Chen, Y.C.; Yang, L.; Zhang, T.; Ju, H.Y. Non-contact harmonic magnetic field detection for parallel steel pipeline localization and defects recognition. *Measurement* **2021**, *180*, 109534. https://doi.org/10.1016/j.measurement.2021.109534.
53. Cui, P.; Zhu, W.B.; Ji, H.J.; Chen, H.T.; Hang, C.J.; Li, M.Y. Analysis and optimization of induction heating processes by focusing the inner magnetism of the coil. *Appl. Energy* **2022**, *321*, 119316. https://doi.org/10.1016/j.apenergy.2022.119316.
54. Zhang, X.; Li, W.W.; Li, B.; Tu, J.; Liao, C.H.; Wu, Q.; Feng, S.; Song, X.C. A new design of the dual-mode and pure longitudinal EMAT by using a radial-flux-focusing magnet. *Sensors* **2022**, *22*, 1316. https://doi.org/10.3390/s22041316.
55. Chen, X.D.; Wang, E.H.; Shan, L.K.; Feng, C.; Zheng, Y.; Dong, Y.; Guo, G.C.; Sun, F.W. Focusing the electromagnetic field to $10^{-6}\lambda$ for ultra-high enhancement of field-matter interaction. *Nat. Commun.* **2021**, *12*, 6389. https://doi.org/10.1038/s41467-021-26662-5.
56. Daskalakis, Z.J.; Farzan, F.; Barr, M.S.; Maller, J.J.; Chen, R.; Fitzgerald, P.B. Long-interval cortical inhibition from the dorsolateral prefrontal cortex: A TMS-EEG study. *Neuropsychopharmacology* **2008**, *33*, 2860–2869. https://doi.org/10.1038/npp.2008.22.
57. Li, J.T.; Liang, Z.; Ai, Q.Y.; Yan, X.H.; Tian, J. Double butterfly coil for transcranial magnetic stimulation aiming at improving focality. *IEEE Trans. Magn.* **2012**, *48*, 3509–3512. https://doi.org/10.1109/TMAG.2012.2199474.
58. Rotundo, S.; Brizi, D.; Flori, A.; Giovannetti, G.; Menichetti, L.; Monorchio, A. Shaping and focusing magnetic field in the human body: State-of-the art and promising technologies. *Sensors* **2022**, *22*, 5132. https://doi.org/10.3390/s22145132.
59. Lee, S.W.; Fallegger, F.; Casse, B.D.F.; Fried, S.I. Implantable microcoils for intracortical magnetic stimulation. *Sci. Adv.* **2016**, *2*, e1600889. https://doi.org/10.1126/sciadv.1600889.
60. Philip, N.S.; LaBar, K.S. Mapping a pathway to improved neuropsychiatric treatments with precision transcranial magnetic stimulation. *Sci. Adv.* **2022**, *8*, q7254. https://doi.org/10.1126/sciadv.abq7254.
61. Amigo, I. Stimulating the brain may help people who stutter. *Science* **2022**, *376*, 1365–1366. https://doi.org/10.1126/science.add5967.
62. Wadman, M. Zapping cocaine addiction. *Science* **2017**, *357*, 960–963. https://doi.org/10.1126/science.357.6355.960.
63. Liu, S.W.; Sun, Y.H.; He, L.S.; Kang, Y.H. Magnetic focusing method and sensor in surface topography testing for ferromagnetic materials. *Sens. Actuators A Phys.* **2019**, *285*, 531–542. https://doi.org/10.1016/j.sna.2018.11.055.
64. Passarotto, M.; Qama, G.; Specogna, R. A fast and efficient simulation method for inductive position sensors design. In Proceedings of the 2019 IEEE Sensors of the Conference, Montreal, QC, Canada, 27–30 October 2019. https://doi.org/10.1109/SENSORS43011.2019.8956502.
65. Anandan, N.; Varma Muppala, A.; George, B. A flexible, planar-coil-based sensor for through-shaft angle sensing. IEEE Sens. J. 2018, 18, 10217–10224. https://doi.org/10.1109/JSEN.2018.2874065.
66. Yang, C.; Tian, Y.; Yu, J.; Jin, M.; Xie, N.; Deng, Y. A 3D printing method of customized magnetic focusing generator for magnetic field therapy. Acad. J. Med. Health Sci. 2022, 3, 44–53. https://doi.org/10.25236/AJMHS.2022.030309
67. Anil Kumar, A.S.; George, B. A noncontact angle sensor based on eddy current technique. IEEE Trans. Instrum. Meas. 2020, 69, 1275–1283. https://doi.org/10.1109/TIM.2019.2908508.
68. Liu, C.; Ding, H.; Fang, X.; Wang, Z. Optimal design of transcranial magnetic stimulation thin core coil With trade-off between stimulation effect and heat energy. IEEE Trans. Appl. Supercond. 2020, 30, 1–6. https://doi.org/10.1109/TASC.2020.2978790.
69. Zhang, Z.; Ni, F.; Dong, Y.; Guo, C.; Jin, M.; Liu, H. A novel absolute magnetic rotary sensor. IEEE Trans. Ind. Electron. 2015, 62, 4408–4419. https://doi.org/10.1109/TIE.2014.2387794
70. Liu, J.; Lu, J.; Liu, C.; Hu, Y. Coil arrays modeling and optimization for transcranial magnetic stimulation. In Proceedings of the 2009 2nd International Conference on Biomedical Engineering and Informatics, Tianjin, China, 17–19 October 2009; pp. 1–5. https://doi.org/10.1109/BMEI.2009.5305488.
71. Wu, Y.X.; Yu, H.Y.; Liu, Z.W. Numerical investigation of the magnetic and electric field distributions produced by biconical transcranial magnetic stimulation coil for optimal design. IEEE Trans. Magn. 2018, 54, 1–5. https://doi.org/10.1109/TMAG.2018.2850915.
72. Zhang, X.; Wang, Y. Calculation of transient magnetic field and induced voltage in photovoltaic bracket system during a lightning stroke. *Appl. Sci.* **2021**, *11*, 4567. https://doi.org/10.3390/app11104567.
73. Zhang, G.Z.; Chen, K.; Li, X.H.; Wang, K.; Fang, R.X.; Liu, J.B. Flexible built-in miniature Archimedes spiral antenna sensor for PD detection in GIS. *High Volt. Eng.* **2022**, *48*, 2244–2254. https://doi.org/10.13336/j.10036520.hve.20210634.3.
74. Song, Z.H.; Zhang, J.; Liu, M.J. Hemispherical Archimedean spiral antenna for multi-mode satellite navigation signals receiving. *J Astronaut.* **2010**, *31*, 391–396. https://doi.org/10.3873/j.issn.1000-1328.2010.02.0155.
75. Aditya, K. Analytical design of Archimedean spiral coils used in inductive power transfer for electric vehicles application. *Electr. Eng.* **2018**, *100*, 1819–1826. https://doi.org/10.1007/s00202-017-0663-7.
76. Rodríguez-Maldonado, J.; Posadas-Castillo, C.; Zambrano-Serrano, E. Alternative method to estimate the Fourier expansions and its rate of change. *Mathematics* **2022**, *10*, 3832. https://doi.org/10.3390/math10203832.
77. Pachuau, J.L.; Kashyap, P.; Kumar, A.; Paul, R.; Id, P.; Chandrakiran, B.; Debnath, S.; Saha, A.K. Segmentation of composite signal into harmonic Fourier expansion using genetic algorithm. *Int. J. Inf. Technol.* **2022**, *14*, 3507–3515. https://doi.org/10.1007/s41870-022-00944-7.
78. Liang, Z.G.; Tang, R.Y. Analytical solution of eddy current loss in core of an electromagnetic valve. *Proc. CSEE* **2005**, *25*, 153–157. https://doi.org/10.13334/j.0258-8013.pcsee.2005.09.028.

79. Jiao, S.; Liu, X.; Zeng, Z. Intensive study of skin effect in eddy current testing with pancake coil. Ieee T Magn 2017, 53, 1-8 DOI: 10.1109/TMAG.2017.2669181
80. Mirrashid, M.; Naderpour, H. Incomprehensible but Intelligible-in-time logics: Theory and optimization algorithm. *Knowl.-Based Syst.* **2023**, *264*, 110305. https://doi.org/10.1016/j.knosys.2023.110305.
81. Mirrashid, M.; Naderpour, H. Transit search: An optimization algorithm based on exoplanet exploration. *Results Control Optim.* **2022**, *7*, 100127. https://doi.org/10.1016/j.rico.2022.100127.
82. Hoxha, A.; Passarotto, M.; Qama, G.; Specogna, R. Design optimization of PCB-Based rotary-inductive position sensors. *Sensors* **2022**, *22*, 4683. https://doi.org/10.3390/s22134683.
83. Sharmin, S.; Ahmedy, I.; Md Noor, R. An energy-efficient data aggregation clustering algorithm for wireless sensor Networks using hybrid PSO. *Energies* **2023**, *16*, 2487. https://doi.org/10.3390/en16052487.
84. Shami,T. M.; El-Saleh,A. A.; Alswaitti, M.; Al-Tashi, Q.; Summakieh, M.A.; Mirjalili, S. Particle swarm optimization: A comprehensive survey. *IEEE Access* **2022**, *10*, 10031–10061. https://doi.org/10.1109/ACCESS.2022.3142859.
85. Wang, J.; Wang, X.; Li, X.; Yi, J. A hybrid particle swarm optimization algorithm with dynamic adjustment of inertia weight based on a new feature selection method to optimize SVM parameters. *Entropy* **2023**, *25*, 531. https://doi.org/10.3390/e25030531.
86. Anandan, N.; George, B. Design and development of a planar linear variable differential transformer for displacement sensing. *IEEE Sens. J.* **2017**, *17*, 5298–53051. https://doi.org/10.1109/JSEN.2017.2719101.
87. Wang, K.; Zhang, L.S.; Le, Y.; Zheng, S.Q.; Han, B.C.; Jiang, Y.X. Optimized differential self-inductance displacement sensor for magnetic bearings: Design, analysis and experiment. *IEEE Sens. J.* **2017**, *17*, 4378–4387. https://doi.org/10.1109/JSEN.2017.2710135.
88. Fonte, M.; Duarte, P.; Anes, V.; Freitas, M.; Reis, L. On the assessment of fatigue life of marine diesel engine crankshafts. *Eng. Fail. Anal.* **2015**, *56*, 51–57. https://doi.org/10.1016/j.engfailanal.2015.04.014.
89. Li, R.; Wen, C.W.; Meng, X.H.; Xie, Y.B. Measurement of the friction force of sliding friction pairs in low-speed marine diesel engines and comparison with numerical simulation. *Appl. Ocean Res.* **2022**, *121*, 103089. https://doi.org/10.1016/j.apor.2022.103089.
90. Tawadros, P.; Awadallah, M.; Walker, P.; Zhang, N. Using a low-cost bluetooth torque sensor for vehicle jerk and transient torque measurement. *Proc. Inst. Mech. Eng. Part D* **2019**, *234*, 423–437. https://doi.org/10.1177/0954407019861613.
91. Gryz, K.; Karpowicz, J.; Zradziński, P. Complex electromagnetic issues associated with the use of electric vehicles in urban transportation. *Sensors* **2022**, *22*, 1719. https://doi.org/10.3390/s22051719.
92. Jeranče, N.; Vasiljević, D.; Samardžić, N.; Stojanović, G. A compact inductive position sensor made by inkjet printing technology on a flexible substrate. *Sensors* **2012**, *12*, 1288–1298. DOI：10.3390/s120201288.
93. Losby, J.E.; Sauer, V.T.K.; Freeman, M.R. Recent advances in mechanical torque studies of small-scale magnetism. *J. Phys. D Appl. Phys.* **2018**, *51*, 483001. https://doi.org/10.1088/1361-6463/aadccb.